Fuel 357 (2024) 130030

Contents lists available at ScienceDirect

Fuel

journal homepage: www.elsevier.com/locate/fuel

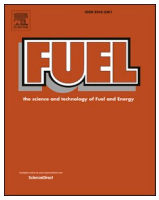

Full Length Article

A novel bound water occurrence model for tight sandstone

Zezhang Song [a,b,*], Lv Mingyang[a,b], Zhao Libin[a,b,c], Liu Changqi[a,b], He Yuanyuan[c], Zhang Yueqiao[d], M.A. Lobusev[e]

[a] National Key Laboratory of Petroleum Resources and Engineering, China University of Petroleum (Beijing), Beijing 102249, China
[b] College of Geosciences, China University of Petroleum (Beijing), Beijing 102249, China
[c] Research Institute of Petroleum Exploration & Development of PetroChina Tarim Oilfield Company, Xinjiang Korla 841000, China
[d] Research Institute of Petroleum Exploration and Development, Petro China, Beijing 100083, China
[e] Faculty of Petroleum Geology and Geophysics, RSU of Oil and Gas (NIU) named after I.M.Gubkin, Moscow 119991, Russian Federation

ARTICLE INFO

Keywords:
Water-film
Bound water
Ultra-deeply-buried
Pore structure
Bashijiqike tight sandstone

ABSTRACT

Understanding the occurrence state and microscopic distribution of bound water, as well as the factors governing bound water saturation and its impact on natural gas flow within nano-scaled pore networks, holds significant importance for reservoir evaluation, productivity prediction, and production. However, the complexity of pore structure poses a challenge in quantitatively characterizing these aspects, and currently, no effective method exists to achieve this characterization. This study takes the Bashijiqike tight sandstone of the Kuqa Depression of the Tarim Basin as an example; by integrating physical property test, XRD, microscopic observation with casting thin section and SEM, HPMI, NMR, and NMR-supervised gas-charging experiment, proposed a novel bound water occurrence model to depict the microscopic distribution of bound water in nano-scaled pore space. Furthermore, the impact of bound water on gas-flowing behaviors was thoroughly examined and the complex relationships between bound water saturation and reservoir macroscopic and microscopic parameters were explored. In addition, based on the grey relational analysis, the critical controlling factor on bound water saturation were screened out.

The bound water in the pore space of tight sandstone comprises two components: capillary-bound water within small pores ($<r_{cutoff}$) and restricted (by pore/throat $< r_{cutoff}$) large pores, layered water-film within large pores ($>r_{cutoff}$). The water-film within large pores is non-uniform, non-isothick, and low in content. During gas charing to reservoirs, the water-film thickness decreased gradually as the charging force increased, with a minimum thickness ranging from 0.10 to 3.72 nm. Water-film accounted for 1.75% to 22.96% of the total bound water content, with an average of 7.28%. In contrast to previous studies, we found that water-film had a negligible impact on the minimum pore/throat radius for gas charging, with only an increase of 0.7 nm. However, it significantly altered the physical characteristics, reducing gas permeability from 46.11% to 97.84%, with an average reduction of 78.37%. Furthermore, a water-film effectively eradicated the slip effect, leading to the prevalence of Darcy and diffusion flow as the primary mechanisms for gas seepage. At low pressure, diffusion flow prevails, whereas Darcy flow dominates at high pressure. I/S-mixed layer and illite exert the most significant influence on bound water saturation.

1. Introduction

The geological reserves of China's tight sandstone gas totaled 20.9 × 10^{12} m^3 in 2020, making it the unconventional natural gas with the highest proven rate (30.9%) [1]. From the perspective of technically recoverable reserves, proven reserves, and production, tight sandstone gas is the most realistic unconventional natural gas that should be exploited first in China [2].

The fluid in tight sandstone reservoirs is typically classified into bound water and movable fluid based on their occurrence states. In contrast to bound water, the movable fluid holds industrial significance [3]. However, due to nano-scaled pore size, robust heterogeneity, and complicated pore network, tight sandstone always contains a large amount of bound water [4]. In previous studies, the bound water

* Corresponding author at: National Key Laboratory of Petroleum Resources and Engineering, China University of Petroleum (Beijing), Fuxue Road No. 18, Changping, Beijing 102249, China.
E-mail address: songzz@cup.edu.cn (Z. Song).

https://doi.org/10.1016/j.fuel.2023.130030
Received 25 July 2023; Received in revised form 22 September 2023; Accepted 4 October 2023
Available online 9 October 2023

saturation of typical tight sandstone gas reservoirs was reported to be 25.82%-81.15% in the Yanchang Formation in the Ordos Basin, 20%-60% in the Xujiahe Formation in the Sichuan Basin, and 13.5%-57.93% in the Bashijiqike Formation in the Tarim Basin [5–7]. Therefore, the gas recovery for tight sandstone is still incredibly low (between 5% and 10%) even after massive horizontal drilling and substantial hydraulic fracturing [8]. Therefore, a thorough comprehension of bound water micro-distribution in pore space and its effect on gas-flowing behaviors, the critical controlling factors on bound water, is imperative for reservoir evaluation, productivity prediction, and gas recovery.

Two conventional models have been proposed to explain the occurrence of bound water in pore space, which is currently extensively utilized: the capillary-bound water model (Fig. 1a) and the water-film-bound water model (Fig. 1b) [9]. The capillary-bound water model postulates that the occurrence of bound water is governed by capillary force—bound water only saturated in relatively small pores and does not exist in large pores [10,11]. Compared to the capillary-bound water model, the water-film-bound water model is a more viable option for long-term practical applications [12]. The concept of bound water as a water-film in pore space was proposed as early as the 1950s [13]. Nonetheless, a precise definition of the occurrence and thickness of water-film remains elusive(Fig. 1). At first, scholars assumed that all pores contain a layer of bound water-film (Fig. 1b) regulated by electrochemical forces [14]: polar water molecules close to the particle surface generate an electrostatic field, resulting in an ordered arrangement of water molecules [15]. Regarding the thickness of the water-film, a widely accepted consensus was that it possessed a relatively uniform and consistent thickness, ranging from 0.05 to 1 μm [16], occupying a significant portion of the pore volume [17].

Also, some scholars even once treated the capillary-bound water as a water-film: during oil and gas-charging into nano-scaled pore networks, if the pore/throat radius was so small that hydrocarbon could not charge into pore space successfully, then the capillary-bound water in small pores/throats was treated as water-film [18]. The charging of hydrocarbons into pore space is contingent upon the pore radius surpassing the thickness of the water-film [19,20]. In this case, the water-film is equivalent to capillary-bound water.

Since the turn of the 21-st century, an increasing number of researchers related the occurrence of bound water with hydrocarbon charging and posited that bound water should consist of two distinct components (Two-component bound water model) (Fig. 1c): capillary-bound water in small pores and water-film in large pores [21]. In this context, large pores were defined as those with a radius of more than 50 nm [22]. Furthermore, the corresponding thickness of the water-film in large pores was also considered uniform and consistent, ranging from 0.01 to 0.05 μm [15,23]. Worth noting, with the increasing application of molecular dynamics simulation in the petroleum industry in recent years, more and more scholars suggested that the water-film's thickness should be thinner and more heterogenous, which should be restricted to several multiples of the water molecule diameters, approximately 0.7 nm [24,25]. Additionally, the stability and thickness of the nano-scaled water-film are significantly influenced by solid-liquid interactions [26], including Van der Waals force, electrostatic force etc.

Indeed, to date, the industry has not reached a consensus on the bound water occurrence state in the pore space. The occurrence of bound water is important in the following aspects: (1) It determines the minimum effective pore/throat radius for gas-charging during hydrocarbon accumulation [18,27]. Researchers commonly perceived the water-film thickness as the minimum effective pore/throat radius. Only when the pore/throat radius surpasses the water-film thickness can the pore/throat serve as an efficient charging pathway for tight gas accumulation. Nevertheless, employing a water-film-bound water model in this particular framework results in a relatively substantial calculated water-film thickness. Consequently, this will significantly augment the minimum effective pore/throat radius for gas-charging during hydrocarbon accumulation and amplify the influence of the water-film on the lower gas-charging limit. (2) It affects the physical properties of tight sandstone reservoirs [15]. Wang (2020) 's research revealed that as water saturation increases, the permeability of tight sandstone samples decreases exponentially [28]. However, previous studies have primarily focused on the correlation between bound water saturation and permeability, neglecting the influence of different types of bound water or the occurrence of bound water in pore space. (3) The bound water occurrence also profoundly impacts gas-flowing behaviors within

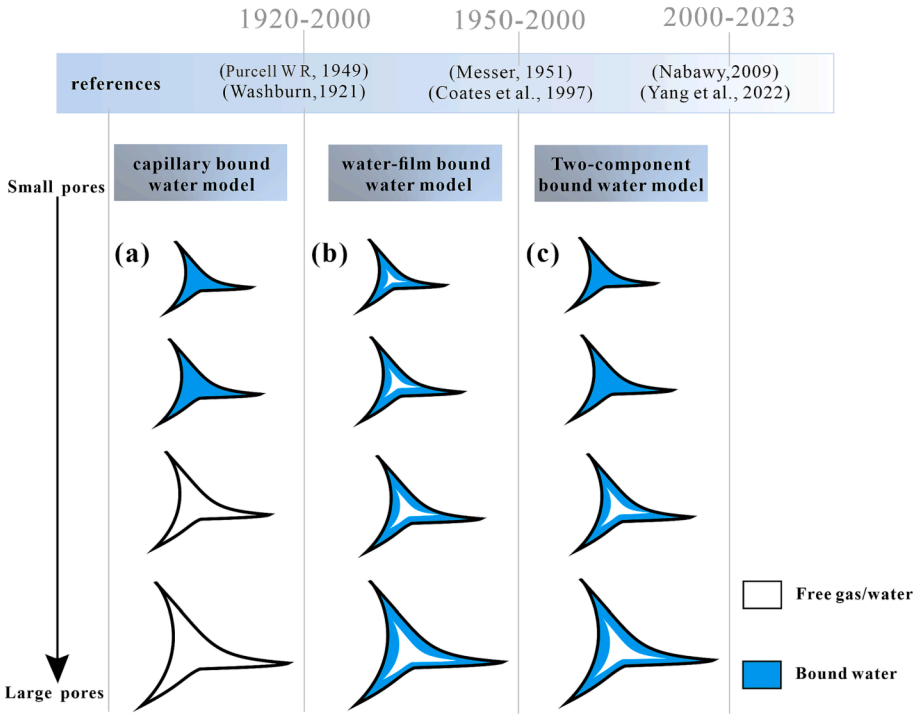

Fig. 1. The evolution of bound-water occurrence models.

nanopores under confinement conditions [17,29]. An essential inquiry arises concerning the phase in which natural gas traverses the confined nanoporous environment. Prior research has shown that when methane flows through quartz nanopores, slip flow occurs, whereas if a water-film is present in the pore network, methane's flow adheres to Darcy's Law and can be categorized as bulk flow [30]. However, the pore/throat size distribution (PSD) obtained from nuclear magnetic resonance (NMR) experiments often reveals a phenomenon that bulk phase flow cannot adequately explain—movable gas exists in small pores beyond the influence of corresponding charging forces.

Regarding the controlling factors on bound water saturation, mineral composition and the pore structure [10] of the reservoirs were considered as the fundamental factors; also, reservoir physical properties and microscopic heterogeneity were frequently discussed [31,32]. However, the high bound water saturation observed in tight sandstone reservoirs is a consequence of the combined influence of multiple factors rather than being solely attributed to a single reservoir property. Furthermore, previous research primarily investigated the linear correlation between bound water saturation and various geological factors to analyze the underlying geological causes [33]. However, it is essential to note that the relationship between bound water saturation and these factors is often complex and nonlinear, making it challenging to accurately represent its inherent connection using conventional linear models. Numerous findings indicate a limited linear correlation between bound water saturation and diverse factors [34]. Moreover, the linear correlation outcomes between the same geological factors and bound water saturation exhibit significant variations across different regions [35,36]. Therefore, judging whether a specific factor controls tight sandstone's bound water saturation is challenging.

As the research object, we selected one of China's most typical tight sandstones, the Bashijiqike tight sandstone in the Kuqa Sag of the Kelasu structural belt in the Tarim Basin. The Bashijiqike tight sandstone is characterized by diverse mineral compositions, poor physical properties, strong microscopic heterogeneity, complex microscopic pore structure, and high bound water saturation [37–39]. By integrating physical properties test, XRD, SEM, HPMI, NMR, and NMR-supervised gas-charging experiment, this study aims at (1) proposing the microscopic occurrence model of bound water in the pore space of tight sandstone; (2) exploring the influence of bound water occurrence on gas-flowing behaviors under the proposed bound water occurrence model; (3) analyzing the key factors controlling the bound water saturation.

2. Geologic setting and sampling

Kuqa depression is located north of Tarim Basin and distributed in the northeast direction, with an area of about 3.7 × 10^4 km^2 [40]. Its north edge is the South-Tianshan Orogenic Belt, and its south is adjacent

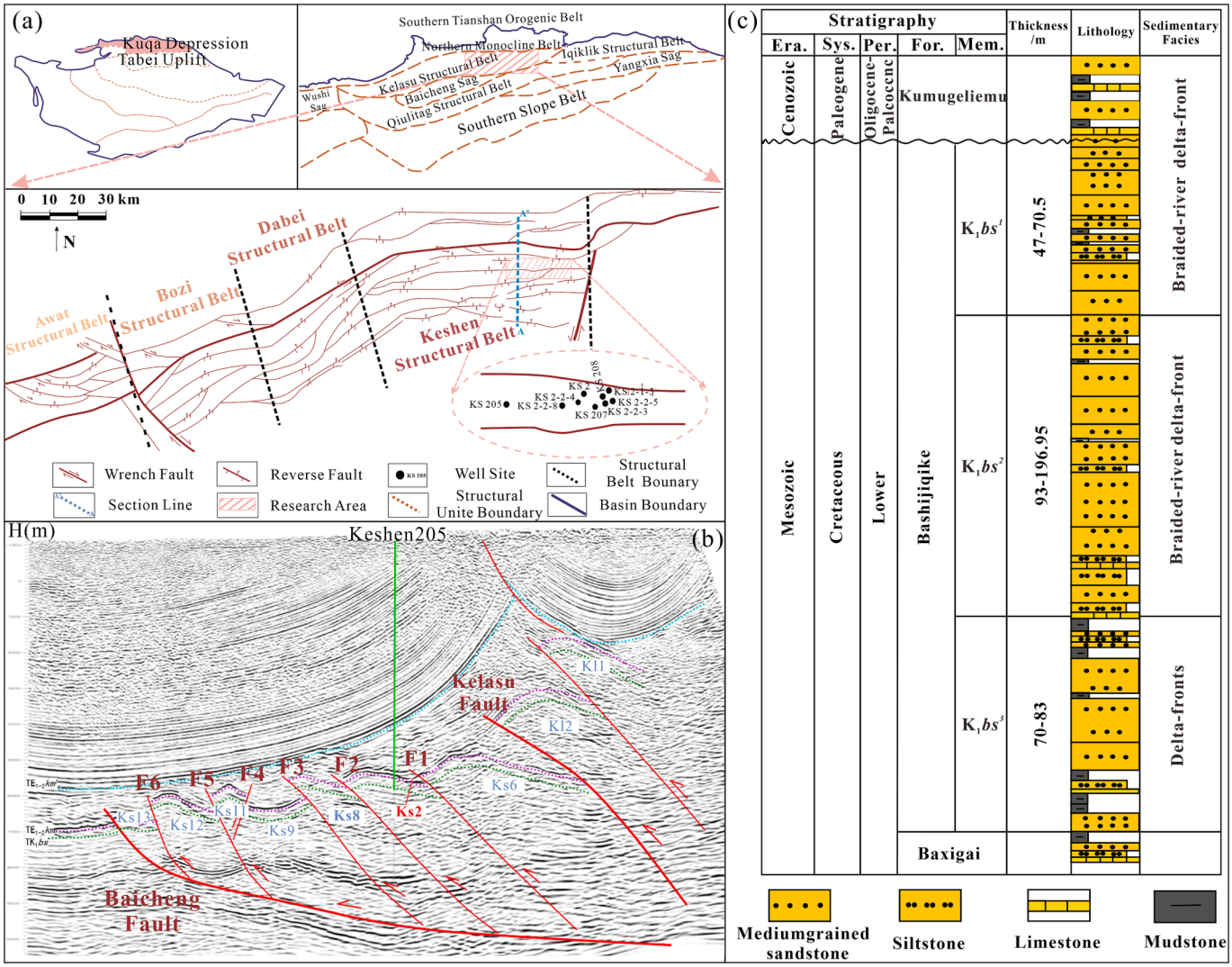

Fig. 2. Geologic background of the research area.

to the Tabei uplift. Kuqa depression includes eight secondary structures: the Northern Monoclinal Belt, Kelasu Structural Belt, Iqiklik Structural Belt, Baicheng Sag, Yangxia Sag, Wushi Sag, Qiulitage Structural Belt, and Southern Slope Belt. The Kelasu Structural Belt develops a series of thrusting faults from North to South and fault-related folds spreading nearly east-west, with the characteristics of "East-West segmentation and Vertical stratification" [41]. From west to East of the Kelasu Structural Belt, there are apparent differences in structural deformation, based on which the Kelasu Structural Belt can be divided into Awat, Bozi, Dabei, and Keshen secondary structural belts (Fig. 2-a).

The Keshen structural belt is located in the Middle East of the Kelasu structural belt. It extends about 50 km from west to East. Compared with other secondary structural belts, a relatively well-developed thrust imbricate structure characterizes the Keshen structural belt, and the faults and anticlines developed therein are favorable traps for oil and gas accumulation [41]. In addition, the Keshen structural belt's structural characteristics are mainly controlled by the Kelasu Fault on the northern border and the Baicheng Fault on the southern border. Six secondary faults (F1, F2, F3, F4, F5, F6) are developed between these two boundaries, dividing the Keshen structural belt into seven secondary fault blocks and the Kela2 fault block in the north of the Kelasu fault. The study area, the Keshen2 fault block, is controlled by F1 and F2 faults (Fig. 2-b).

The strata from top to bottom in the Keshen structural belt include the Quaternary system (Q), Neogene Kuqa (N_2k), Kangcun ($N_{1\text{-}2}k$), and Jidik (N_1j) Formations, Paleogene Suweiyi ($E_{2\text{-}3}s$) Formation and Kumgelemu Group ($E_{1\text{-}2}km$), Cretaceous Bashijiqikee (K_1bs), Baxigai (K_1bx) and Shushanhe (K_1sh) Formations. Among them, the Cretaceous Bashijiqikee Formation is the main gas–bearing interval, whose lithology is mainly red to brown, fine to medium-grained sandstone mixed with conglomerates. Bashijiqikee Formation is in angular unconformity contact with the gypsum–salt of the overlying Kumgelemu Group and conformity contact with the underlying Cretaceous Baxigai Formation. The total thickness of the sand body of it is 210 m–350 m.

The Cretaceous Bashijiqikee Formation can be divided into three members from top to bottom (Fig. 1-c), namely, the first (K_1bs^1), second (K_1bs^2), and third (K_1bs^3) members. The first member (K_1bs^1) comprises brown to dark brown, medium-thick sandstone interbedded with thin to medium-thick mudstone, with a thickness of 47–70.5 m. The first member is in unconformity contact with the overlying gypsum salt caprock Kumgeliemu group ($E_{1\text{-}2}km$) and is dominated by braided-river delta-front subfacies. The lithology of the second member (K_1bs^2) is characterized by dark brown, thick to ultra-thick mudstone, silty mudstone, and siltstone, with a thickness of 93–196.5 m. Braided-river delta-front subfacies also dominate the second member. The third member (K_1bs^3) is rich in medium-thick fine-grained sandstone, thin mudstone, and silty mudstone, with a 70–83 m thickness. The third member is in conformal contact with the underlying Baxigai (K_1bx) Formation and is dominated by the delta-front subfacies [42].

This research selected 23 sandstone coring samples from seven exploration wells in the Keshen2 Gas Field for investigation. All samples are from the first and second members of the Bashijiqike Formation, with burial depths ranging from 6600 to 6900 m. Before tests, the salt and residual oil within the samples were extracted using a mixed solution of alcohol and trichloromethane for about 15 days and then dried for 24 h at 120 °C. After that, the dried core plugs were vacuumed for 24 h.

3. Methodology

3.1. Experiments

3.1.1. Thin section observation, SEM, XRD, and physical properties

The physical test for porosity and permeability of all plug samples was carried out by using the CMS-300 from CoreLab, USA.

All tight sandstone samples were cut and polished to 30–35 μm in thickness and glued onto a thin section glass slide. Images were acquired by the Zeiss Axio Imager A1M polarizing microscope, and the features of mineral composition and pore networks were evaluated qualitatively.

Before observations, all the tight sandstone samples were coated with a thin film of gold and palladium and observed under FEI Quanta 250 FEG scanning electron microscope. The images were acquired for each sample.

XRD was carried out by using a D5000 X-ray diffractometer. According to the XRD internal standard, the 18 Bashijiqike samples were milled until the size of 70–80 μm, mixed with ethanol, and smeared on the glass slides.

3.1.2. Centriguration combined NMR test

The Maran Ultra NMR Analyzer from Oxford Instruments, UK, with a main frequency of 2 MHz, minimum signal-to-noise ratio of 100:1, and echo spacing of 0.6 ms, was used to measure all the Bashijiqike tight sandstone plugs. The core plugs underwent a series of procedures, including oil washing and drying, followed by measurement of porosity and permeability. The core plugs should be vacuumed and saturated with simulated formation water (189098 ppm Nacl) to ensure a fluid saturation level of ≥95%. The weight of the plugs in the water-saturated state was measured and recorded. The plugs should then be secured in a specialized nuclear magnetic core holder and positioned at the center of the magnet's uniform area. The water saturation of the plugs should be tested using T_2 spectrum. Under the centrifugal force of 8.53 MPa, high-speed centrifugation was performed on all the samples, and T_2 spectrum and the corresponding weight of the plugs were recorded in the centrifuged state.

In the case of saturation of the pore space by a single-phase wetting fluid, the bulk relaxation time is negligible compared to the surface relaxation time [43]; additionally, if the static magnetic field is uniform or the gradient magnetic field is small and the echo spacing of the CPMG sequence is sufficiently short, the diffusion relaxation can also be disregarded. Under these circumstances, the transverse relaxation time T_2 can serve as an indicator of the specific surface area [44]:

$$\frac{1}{T_2} \approx \frac{1}{T_{2\text{surface}}} = \mathrm{d}\frac{S}{V} = \mathrm{N}\frac{d}{r}\# \tag{1}$$

where T_2 is the transverse relaxation time, ms; d is the transverse surface relaxation strength, which depends on the pore surface properties, the size of the mineral composition and the properties of the saturated fluid, constant; S/V is the specific surface of individual pores; N is the pore shape factor (for spherical pores, N = 3; for cylindrical pores, N = 2), which is dimensionless; r is the pore radius, μm.

Therefore, the pore size distribution can be obtained by referring to [5]:

$$T_2 = mr^n\# \tag{2}$$

Where m and n is the conversion factor.

3.1.3. NMR-supervised Gas-Charging experiment

The NMR-supervised Gas-Charging Experiment adopts the 0.28T permanent magnet nuclear magnetic resonance imaging analysis equipment (MT-NMR series) produced by Beijing Megtech Technology Development Co., Ltd. The system has a three-dimensional self-shielding water-cooled gradient coil with a maximum gradient field of 300mT/m; 1-inch, 1.5-inch static probe, and 1-inch high temperature and high-pressure core-holder. It can give NMR results like the T_2 spectrum, T_1 spectrum, D-T_2 two-dimensional spectrum, T_1-T_2 two-dimensional spectrum, and rapid 1D/2D/3D imaging functions. The minimum Echo Spacing is 0.6 ms.

We selected three plugs with less than 20% bound water saturation for online NMR-supervised gas-charging experiments. The core plugs were first saturated with simulated formation water. The plugs should then be secured in a specialized nuclear magnetic core holder and

positioned at the center of the magnet's uniform area. Confining pressure should be applied to the formation pressure, followed by nitrogen injection under increasing pressure. The T_2 spectrum should be tested every 30 s, after 5 h, and then every 30 min. If the cumulative area change of T_2 spectrum exceeds 15% over a specified period, NMR 3D imaging is conducted, and plugs are extracted to assess gas permeability. The process is repeated iteratively until the gas outlet exhibits continuous flow at the specified rate and the cumulative area of the T_2 spectrum no longer displays significant changes.

3.2. Water-film related theories and water-film saturation calculation method

3.2.1. Water-film-related theories

(1) Water-film disjoining pressure

The interaction force between water-film and solid surfaces is the key to determining the stability and thickness of adsorbed water-film, which can be quantitatively determined by disjoining pressure Π(*h*). Based on the Derjaguin-Landau-Verwey-Overbee (DLVO), the disjoining pressure is the sum of the three components[45]:

$$\Pi(h) = \Pi_{\mathrm{m}}(h) + \Pi_{\mathrm{e}}(h) + \Pi_{\mathrm{s}}(h) \tag{3}$$

where $\Pi_{\mathrm{m}}(h)$, $\Pi_{\mathrm{e}}(h)$, $\Pi_{\mathrm{s}}(h)$ are the molecular component, electrostatic component, and structural component of disjoining pressure, respectively; MPa.

(2) Molecular force

The molecular force in wetting film systems can be either attractive or repulsive, which mainly depends on the polarization of adsorbed film and solid surface, and it can be expressed as [46]:

$$\Pi_{\mathrm{m}}(h) = -\frac{A}{6\pi h^3} \tag{4}$$

where A is the Hamaker constant, J.

If A_{gws} refers to the Hamaker constant of the solid-water interface and gas-water interface separated by the liquid film, A_{wgw} refers to the Hamaker constant of water-gas interface and gas-water interface separated by liquid film, then they can be given by [47]:

$$A_{gws} \approx \left(\sqrt{A_{gg}} - \sqrt{A_{ww}}\right)\left(\sqrt{A_{ss}} - \sqrt{A_{ww}}\right)\# \tag{5}$$

$$A_{wgw} \approx \left(\sqrt{A_{ww}} - \sqrt{A_{gg}}\right)\left(\sqrt{A_{ww}} - \sqrt{A_{gg}}\right)\# \tag{6}$$

where A_{gg}, A_{ww}, and A_{ss} are the Hamaker constants of gas/gas, water/water, and solid/solid via vacuum, respectively, J. The obtained A_{gws} is about -7.41×10^{-21} J, demonstrating a repulsive between the solid-water and gas-water interfaces. The calculated A_{wgw} is about 3.7×10^{-20} J, indicating an attraction between two similar adsorbed films.

(3) Electrostatic force

The electrostatic component is significantly influenced by the ion concentrations of electrolyte solutions [48]. $\Pi_{\mathrm{e}}(h)$ originates from the compression of the electric double layer into a confined space. To describe the water-film thickness for a low-concentration aqueous solution adsorbed on the surface with high electrostatic potential, Langmuir [46] developed the following simple electric double-layer model:

$$\Pi_e(h) = \frac{\varepsilon_r \varepsilon_0}{2}\left(\frac{\pi k_B T}{eZ}\right)^2 \frac{1}{h^2}\# \tag{7}$$

where ε_r is the static relative permittivity of water, ε_0 is the permittivity of free space ($C_2\ J^{-1}\ m^{-1}$), k_B is the Boltzmann constant ($J\ K^{-1}$), e is the electron charge (C), and Z is the ion valence.

(4) Structural force

The attraction or repulsion between two surfaces caused by the overlap of structurally altered boundary layers is referred to as structural forces (also known as hydration force), which can be approximately described by a semi-empirical equation [45]:

$$\Pi_{\mathrm{s}}(h) = k e^{-\frac{h}{\lambda}} \tag{8}$$

where k is the coefficient for the strength of structural force, N/m^2; whose value depends on the wettability of solid surfaces. λ is the characteristic decay length, nm; about 1–2 nm. Generally speaking, the structural force of the reservoir is negligible.

Based on DLVO theory and the Young-Laplace equation, water-film stability and thickness can be clarified according to equation (9):

$$\Delta P = P_g - P_w = \Pi(h) + P_{add} = \Pi_m(h) + \Pi_e(h) + \Pi_s(h) + 2H\sigma_{gw}\# \tag{9}$$

where ΔP is the pressure difference between gas and water phases; P_g is the gas phase pressure, MPa; P_w is the water phase pressure, MPa; P_{add} is the capillary pressure caused by gas-water meniscus interface, MPa; H is the average curvature of the solid surface on which the water-film is formed, m^{-1}; σ_{gw} is the gas-water surface tension, mN/m.

3.2.2. Water-film saturation calculation method

Assuming the pore is cylindrical (Fig. 10-d), the pore ratio surface is inversely proportional to the pore radius. Since the water-film exists in large pores, the volume of the large pores with different radii can be calculated by using the NMR PSD (8.53 MPa) before and after the optimal centrifugation force:

$$V_{li} = V \times (\varphi_i - \varphi_{ci})\# \tag{10}$$

where V_{li} is the volume of the large pores with the radius of i, cm^3; V is the volume of sample, cm^3; φ_i is the porosity component of pore with a radius of i, %; φ_{ci} is the porosity component of pore a radius of i after centrifugation, %.

$$S_{li} = \frac{2}{r_i} \times V_{li}\# \tag{11}$$

where S_{li} is the large pore surface area with a radius of i, cm^2.

$$V_{fi} = S_{li} \times h_i\# \tag{12}$$

where V_{fi} *is* the volume of the water-film in the movable fluid pores with a radius of i, cm^3; h_i is the thickness of the water-film within the movable fluid pores with a radius of i.

The bound water-film saturation and capillary-bound water saturation are:

$$S_f = \frac{V_f}{V_p} = \frac{\sum_{i=r_c}^{n} V_{fi}}{V \times \varphi}\# \tag{13}$$

$$S_{cw} = S_b - S_f\# \tag{14}$$

where S_f is bound-water-film saturation, %; V_f is the total volume of bound-water-film,cm^3; V_p is the pore volume of sample, cm^3;r_c is pore radius corresponding to the charging pressure, μm; φ is porosity, %; S_{cw} is capillary bound water saturation, %; S_b is bound water saturation, %.

4. Results

4.1. Physical properties and mineral compositions

The sandstone has undergone strong compaction and cementation

and is characterized by tightness and substantial heterogeneity. The porosity of 23 Bashijiqike samples ranges from 4.13% to 7.45%, with an average and median of 5.27% and 4.97%, respectively. Klinkenberg permeability varies from 0.003 mD to 0.041 mD, with an average value of 0.014 mD and a median value of 0.013 mD. Generally, the Bashijiqike Formation belongs to a typical tight reservoir with ultra-low porosity and permeability (Fig. 3a). In addition, a low correlation between the porosity and logarithm of permeability (R^2 = 0.23) indicates that the Bashijiqike reservoirs exhibit complex pore structures.

The Bashijiqike tight sandstone is mainly composed of feldspar lithic sandstone, with quartz and feldspar as the dominant mineral (Fig. 3b). Quartz content ranges from 43.5% to 60.4%, with an average of 53.9%, while feldspar content ranges from 13.8% to 36.6% with an average of 32.5%. Clay minerals (4.7% to 13.9%, averaging 7.2%) and dolomite (0%−12.3%, averaging 4.4%) follow. There is trace hematite and no calcite. Clay minerals contain 20.3%–38.4% (29.2% on average) illite/smectite mixed layer (I/S mixed layer), 40.7%−51.4% (45.4% on average) illite, 15.7%–37.0% (25.1% on average) chlorite, and almost no kaolinite (Fig. 3c). Overall, the Bashijiqike tight sandstone has a low compositional maturity.

4.2. Microscopic characteristics of pore space

The Bashijiqike tight sandstone in the research area is mainly fine to medium-grained, with moderate sorting. Debris particles are mainly in linear and concave-convex contact (Fig. 4a), indicating a low structural maturity.

The pore space mainly comprises intergranular, dissolution, and intercrystalline pores.

(1) Intergranular pores: the most crucial pore type in the Bashijiqike tight formation. Residual pore spaces formed between particles, primarily triangular or quadrilateral in shape, with straight edges and at micron scale (Fig. 4b-c); filled with authigenic quartz, authigenic feldspar, dolomite, and authigenic/detrital clay.
(2) Dissolution pores: The feldspar in the matrix is dissolved to varying degrees and forms pores of varying sizes and morphologies within or between the particles, forming honeycomb and harbour-shaped pores, mainly at the nano to micron scale (Fig. 4d).
(3) Intercrystalline pores: originated from authigenic clay minerals (authigenic illite, authigenic illite/smectite mixed layer) growing in particle pores in a bridging mode of occurrence, mainly nanopores and it is the main cause of nanoscale porosity (Fig. 4e-f).
(4) Micro-fractures: Interconnected micro-fractures exhibit limited development. Only a few cracks are observed on the particle surface (Fig. 4d). These cracks primarily arise from the compaction and shrinkage of rocks during the diagenetic process and exert a relatively restricted influence on reservoir modification [49].

4.3. Quantitative pore structure characteristics indicated from NMR-related experiments

4.3.1. Pore size distribution from NMR

Centrifugation combined NMR results show that:

(1) The T_2 spectrum's configuration exhibits single, double, and triple peaks (Fig. 5a), signifying a pore structure of considerable complexity.
(2) The NMR PSD (Fig. 5b) yielded from the T_2 test under water-saturated condition show that the Bashijiqike tight sandstone is characterized by nano-scaled pores: the peak position (r_v, Table 1) of the PSD is within the range of 0.0002–0.419 μm (with an average of 0.097 μm); the geometric mean of the pore size (r_{gm}, Table 1) falls within the range of 0.001–0.126 μm (with an average of 0.058 μm); the median pore size (r_{med}, Table1) ranges from 0.001 to 0.130 μm, with an average of 0.057 μm. Pores larger than 1 μm (Fig. 5b) is minimal, with content ranging from 0% to 3.38% (with an average of 1.41%), indicating a lack of developed micro-scaled pores or micro-cracks. The kurtosis (K_G, Table 1) ranges from 0.41 to 0.74 (average 0.54), demonstrating a relatively high concentration of pore size distribution.
(3) The skewness (S_K, Table 1) ranges from 0.75 to 0.96, with an average of 0.87, suggesting a prevailing inclination towards fine skewness. The sorting coefficient (σ, Table 1) varies from 0.81 to 3.29, with an average of 1.81, indicating an overall inadequate sorting. The coefficient of variation (C, Table 1) ranges from 4.00 to 76.20, with an average of 13.17, suggesting a deficient pore structure.
(4) Upon reaching the optimal centrifugation force of 8.53 MPa, the range of T_2 spectrum remains largely unchanged compared to the water-saturated state(Fig. 5 c, d, and e). The bound water saturation (S_b, Table 1) ranges from 16.98% to 50.79%, with an average of 30.57%. Moreover, the bound water content on the right side of the $T_{2cutoff}$ ($T_{2cutoff}$, Table 1) is significantly higher, ranging from 14.11% to 90.56%, with an average of 48.10%, suggesting that irreducible water is not solely confined to small pores, but also exists in large pores, albeit in a higher proportion.

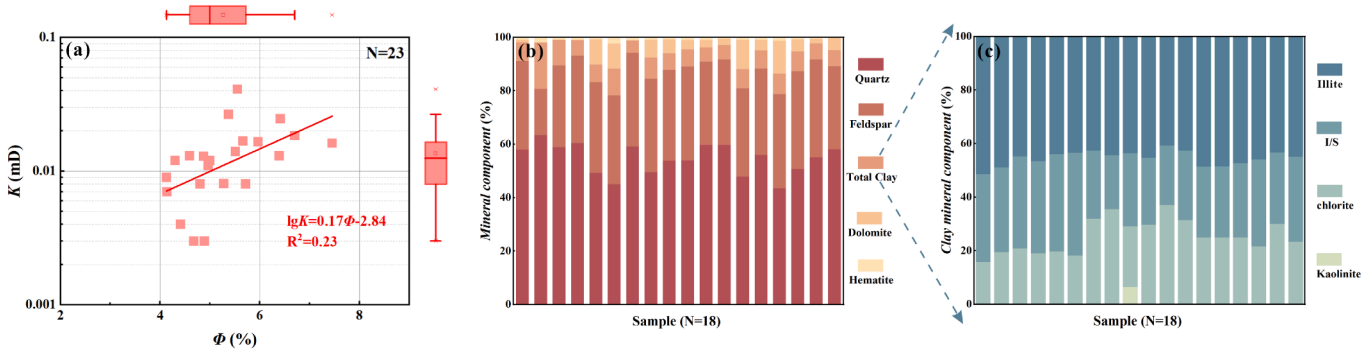

(a) Cross-plot of permeability versus porosity;(b) Mineral composition of the Bashijiqike tight sandstone;(c) Clay mineral composition of the Bashijiqike tight sandstone.

Fig. 3. Petrophysical properties, characteristics, and mineral compositions.

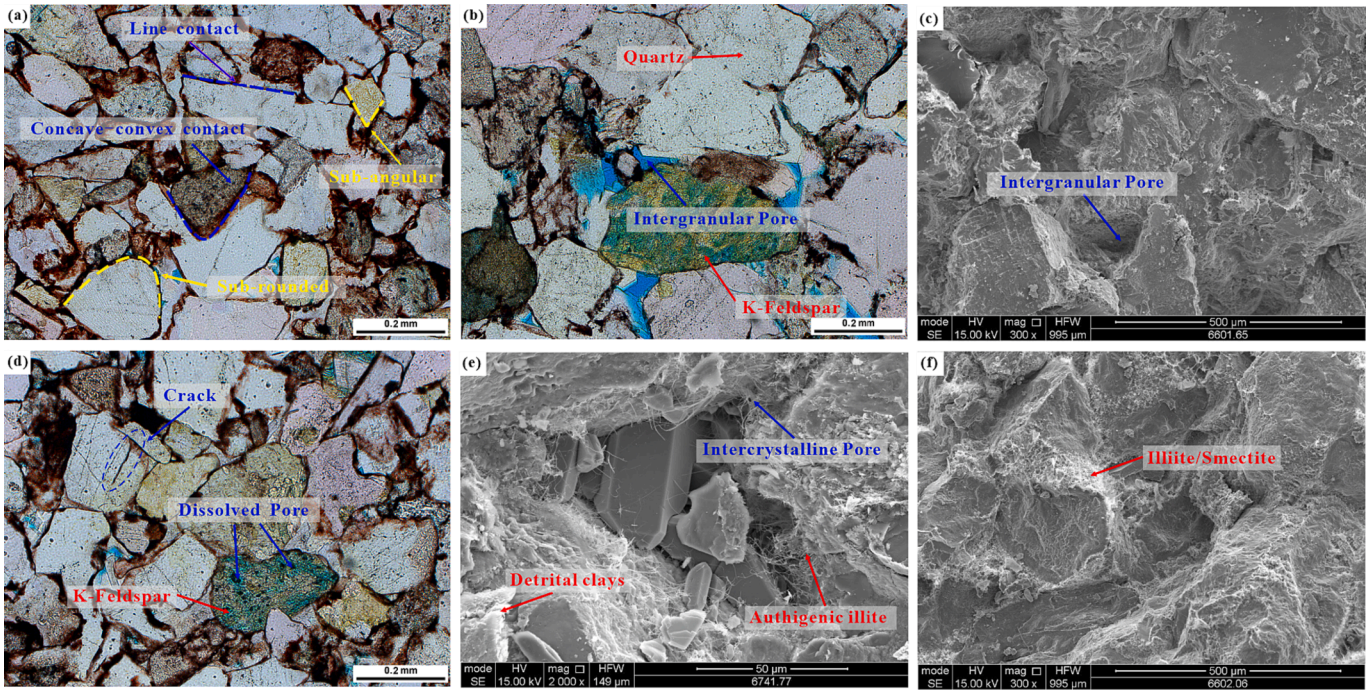

Fig. 4. Pore space observed from thin sections and via SEM for the Bashijiqike tight sandstone.

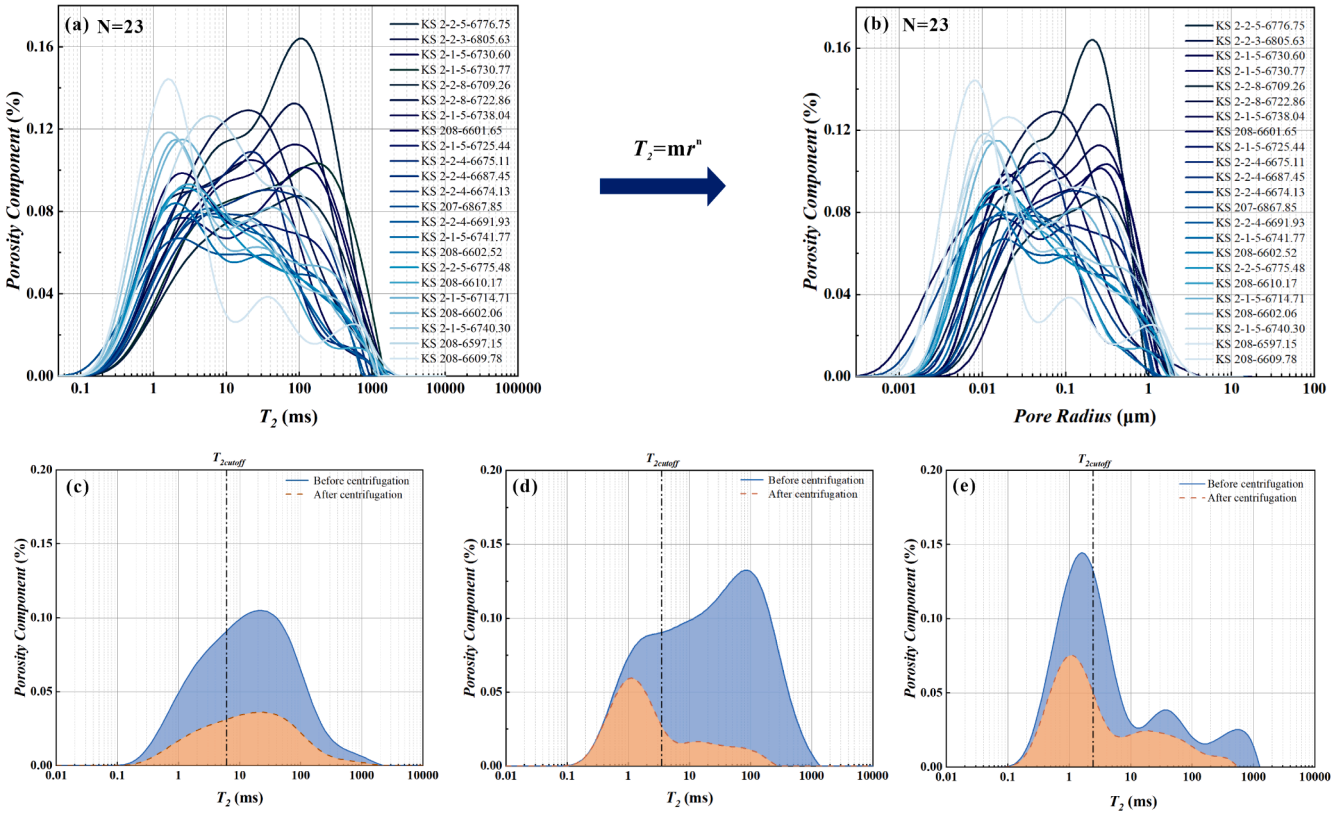

(a) NMR T_2 spectra; (b) NMR PSD ;(c-e)The T_2 spectrum of unimodal, Bimodal, three peaks before and after centrifugation for the sample KS 2-1-5-6738.04, the sample KS 2-2-3-6805.63, the sample Well KS 208-6609.78;

Fig. 5. NMR analysis on the pore structure of the Bashijiqike tight sandstone.

Table 1
Pore structure parameters obtained from the centrifugal NMR experiment.

Samples	$T_{2cutoff}$ ms	K_G	r_v μm	r_{med} μm	$\bar{r}$ μm	r_{gm} μm	S_K	σ	C	S_b %	S_m %
KS 208-6597.15	3.50	0.71	0.020	0.038	0.201	0.045	0.90	3.290	16.340	27.88	72.12
KS 208-6601.65	1.77	0.62	0.419	0.114	0.369	0.112	0.81	2.205	5.982	18.54	81.46
KS 208-6602.06	4.10	0.56	0.012	0.030	0.211	0.042	0.94	2.141	10.161	43.62	56.38
KS 208-6602.52	3.30	0.46	0.012	0.034	0.200	0.043	0.92	2.237	11.209	37.22	62.78
KS 208-6609.78	2.30	0.49	0.008	0.011	0.150	0.018	0.96	2.063	13.789	50.79	49.21
KS 208-6610.17	6.40	0.46	0.015	0.026	0.125	0.031	0.88	1.866	14.951	50.45	49.55
KS 2-2-4-6674.13	3.40	0.42	0.020	0.028	0.116	0.030	0.83	2.360	20.282	29.42	70.58
KS 2-2-4-6675.11	2.00	0.52	0.052	0.030	0.086	0.030	0.80	1.286	14.969	19.3	80.70
KS 2-2-4-6687.45	3.00	0.51	0.126	0.085	0.213	0.085	0.83	1.208	5.679	19.11	80.89
KS 2-2-4-6691.93	3.20	0.44	0.035	0.058	0.182	0.065	0.87	1.212	6.649	26.53	73.47
KS 2-2-8-6709.26	4.80	0.49	0.265	0.119	0.293	0.110	0.81	1.795	6.135	21.4	78.60
KS 2-1-5-6714.71	3.60	0.60	0.015	0.034	0.171	0.043	0.94	1.784	10.425	37.79	62.21
KS 2-1-5-6725.44	2.60	0.51	0.014	0.056	0.220	0.056	0.87	1.686	7.663	26.54	73.46
KS 2-2-8-6722.86	1.80	0.66	0.084	0.065	0.186	0.067	0.81	1.970	10.611	13.50	86.50
KS 2-1-5-6730.6	3.90	0.61	0.258	0.130	0.305	0.126	0.81	1.535	5.032	16.98	83.02
KS 2-1-5-6730.77	4.90	0.56	0.317	0.106	0.265	0.101	0.83	1.275	4.806	21.24	78.76
KS 2-1-5-6738.04	5.80	0.52	0.051	0.030	0.112	0.030	0.79	2.737	24.402	34.38	65.62
KS 2-1-5-6740.3	1.60	0.58	0.010	0.026	0.175	0.036	0.93	1.798	10.276	27.72	72.28
KS 2-1-5-6741.77	5.30	0.44	0.000	0.001	0.023	0.001	0.87	1.722	76.198	42.11	57.89
KS 2-2-5-6775.48	3.70	0.48	0.017	0.034	0.189	0.044	0.92	1.949	10.312	38.43	61.57
KS 2-2-5-6776.75	3.80	0.74	0.203	0.102	0.201	0.089	0.75	0.806	4.009	17.34	82.66
KS 2-2-3-6805.63	3.50	0.73	0.259	0.098	0.237	0.086	0.81	1.466	6.177	24.85	75.15
KS 207-6867.85	15.3	0.41	0.018	0.049	0.184	0.053	0.90	1.276	6.924	57.93	42.07

* K_G = kurtosis (A measure of the sharpness of the PSD,); r_v = the peak position of the PSD, μm; r_{med} = The median pore size, μm; $\bar{r}$=The average pore size, μm; r_{gm} = The geometric mean radius, μm; S_K = Skewness; σ = Sorting coefficient; C = The coefficient of variation($\sigma/\bar{r}$); S_b = The saturation of bound water, %; S_m = The saturation of movable fluid (gas/water), %.

The movable gas/water saturation (S_m, Table 1) ranges from 42.07% to 72.12%, averaging 69.43%.

4.3.2. *Fractal characterization of pore network heterogeneity based on NMR T_2 data*

Fractal analysis on the NMR T_2 data for pore structure heterogeneity characterization of the Bashijiqike tight sandstone was carried out using the wetting-phase fractal model [50]: data points are close to segmental linear distribution on log-log coordinates (Fig. 6), indicating that in different pore size range, the pore structure has different fractal characteristics. Therefore, piecewise fractal analysis is required.

We incorporated a new parameter, r_{cutoff}, denoting the pore radius associated with the charging force as per the Washburn equation to investigate the hydrocarbon accumulation mechanism. Pores possessing a pore radius below r_{cutoff} are classified as small pores, wherein the capillary force impedes the passage of gas, leading to the occupation of these pores by capillary-bound water. Conversely, pores with a pore radius larger than r_{cutoff} are large pores.

In our NMR experiment (with centrifugation), the optimal centrifugation force was set at 8.53 MPa. Thus, the corresponding pore radius is 11.72 nm. We set the logarithm of 11.72 nm as the point of division for the piecewise fractal analysis. Then, the fractal dimensions of large pores (D_L) and small pores (D_S) were calculated, respectively. Results show that D_S (Table 2) is less than 2, demonstrating that small pores do not have fractal characteristics or can not be reasonably explained by

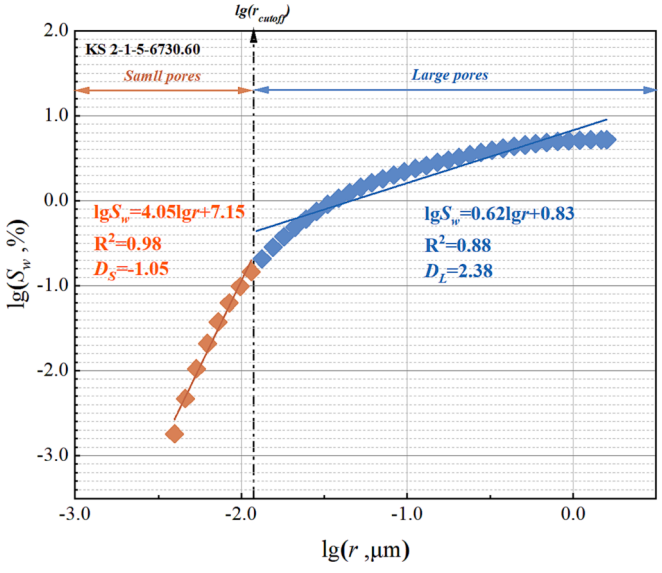

Fig. 6. Fractal analysis on the pore structure of Bashijiqike tight sandstone of the KS2 gas reservoir.

Table 2
The results of the piecewise fractal analysis on the pore structure of the Bashijiqike tight sandstone.

Samples	D_S	R^2	D_L	R^2
KS 208-6597.15	0.53	0.91	2.79	0.88
KS208-6601.65	−0.57	0.96	2.65	0.95
KS 208-6602.06	0.1	0.93	2.79	0.91
KS 208-6602.52	0.03	0.92	2.77	0.91
KS 208-6609.78	0.43	0.9	2.91	0.92
KS 208-6610.17	−0.15	0.92	2.79	0.83
KS 2-2-4-6674.13	0.96	0.92	2.8	0.86
KS 2-2-4-6675.11	0.51	0.94	2.72	0.84
KS 2-2-4-6687.45	−1.17	0.95	2.5	0.91
KS 2-2-4-6691.93	−1.02	0.95	2.58	0.88
KS 2-2-8-6709.26	−0.95	0.96	2.49	0.91
KS 2-1-5-6714.71	0.03	0.93	2.76	0.9
KS 2-1-5-6725.44	−0.26	0.94	2.69	0.92
KS 2-2-8-6722.86	0.4	0.96	2.66	0.86
KS 2-1-5-6730.6	−1.05	0.98	2.38	0.88
KS 2-1-5-6730.77	−0.63	0.96	2.49	0.92
KS 2-1-5-6738.04	0.97	0.89	2.82	0.81
KS 2-1-5-6740.3	−0.04	0.91	2.8	0.9
KS 2-1-5-6741.77	−0.46	0.95	2.72	0.82
KS 2-2-5-6775.48	−0.05	0.94	2.76	0.88
KS 2-2-5-6776.75	−0.58	0.96	2.43	0.93
KS 2-2-3-6805.63	−0.9	0.94	2.58	0.92
KS 207-6867.85	0.14	0.94	2.67	0.92

this fractal model; D_L (Table 2) varies between 2.38 and 2.91 (averaging 2.68), indicating that large pores are with strong heterogeneity.

4.3.3. Seepage characteristics reflected by gas-charging experiment

Online gas-charging experiment shows that (Table3):

(1) Prior to gas-charging, when the core plugs were 100% saturated with formation water, the relative permeability of water of Bashijiqike tight sandstone (Fig. 7 Top-Right) was less than 1, indicating the presence of immovable water within the pore space. When the charging pressure increased to 0.05–0.15 MPa (average 0.12 MPa), and the corresponding water saturation (S_{bc}) ranged from 80.5% to 87.3% (average 84.1%), the gas permeability surpassed 0, signifying a displacement pressure of 0.05–0.15 MPa (average 0.12 MPa) and a maximum connected pore radius of 0.6667–2.00 μm (averaging 1.1111 μm).
(2) With the gradual increase in charging force (from 0 to 8.53 MPa), the amplitude of NMR PSD (Fig. 7 Left) and water saturation (Fig. 7 Right) exhibit a continuous decrease, ultimately reaching equilibrium at around 8.53 MPa. Concurrently, the gas permeability demonstrates a gradual upward trend. Notably, within the displacement force range of 0.15–0.95 MPa, the gas permeability experiences a tenfold increase, while the relative permeability undergoes the most significant enhancement, demonstrating that the 0.1053–0.6667 μm pore/throat and its interconnected pores are decisive in determining the seepage capacity.
(3) The ultimate bound water saturation (S_b, Table 3) after gas-charging exhibits a notable range of values from 13.5% to 20%, with an average of 17.6%. The gas's relative permeability reaches its maximum value ($K_{rg\text{-max}}$, Table 3) within the range of 0.2097–0.5388, with an average of 0.3186. Gas relative permeability below 1 implies that the gas cannot displace a portion of water, consequently affecting gas-flowing behaviors.

5. Discussion

5.1. Quantitative characterization of the occurrence state of bound water

5.1.1. The rationality of the two-components bound water model

The NMR PSDs obtained from gas-charging experiment indicate the presence of bound water in both small (the blue-colored area in Fig. 8) and large pores (the teal-colored area in Fig. 8). The existence of bound water in large pores can be attributed to ink-bottle pores [39]: fluid residing within these large pores can not overcome the capillary force of the small pores interconnected to large pores, subsequently, been "locked" in large pores. The ink-bottle pore structure can also be observed in the casting thin section images.

Moreover, NMR PSDs under the charging forces from 0.15 MPa to 2.13 MPa are higher than the initial water-saturated state in the range of small pores (sky-blue-colored area). The cause behind this anomaly in the left amplitude of the NMR PSD remains unresolved, requiring further explanation.

Functional hydrophilic groups strongly influence water adsorption; these oxygen-containing groups form hydrogen bonds with water molecules and act as main adsorption centers [45]. In addition, many negative charges accumulate on the surface of mineral particles. Since water molecules are polar, water molecules close to the particle surface can form an electrostatic field, resulting in an oriented arrangement of water molecules [15]—a layer of water-film on the particle surface [9]. As water-film in large pores can not be removed in the gas-charing experiment [51], the remaining water-film in the large pores also produces a relaxation signal when performing NMR measurement. As the water-film thickness is much smaller than the pore radius, the relaxation produced by the water-film differs significantly from that when the corresponding pore space was 100% water-saturated [9]. Thus, the relaxation signals generated by the water-film will be reflected in the small pore range, which results in the left amplitude abnormality (the sky-blue-colored area in Fig. 8) of the NMR PSD during the gas-charging experiment. From another perspective, this finding confirms the existence of a water-film within the large pores.

Table 3
Parameters obtained from the online gas-charging experiment.

Samples	K_w/ K_{rg}(100%)	Displacement pressure MPa	S_{bc} %	Maximum connected pore radius μm	Charging force MPa	S_b %	K_g mD	K_{rg}	Gas flow pore space μm
KS208-6601.65 (Φ:6.42%; K:0.0247mD)	0.0007/ 0.0288	0.05	87.3	2	0	100	0.00000	0.00000	–
					0.15	76.5	0.00030	0.01215	>0.6667
					0.46	68.3	0.00050	0.02024	>0.2174
					0.95	51.5	0.00160	0.06478	>0.1053
					2.13	44.8	0.00224	0.09069	>0.0470
					3.79	37.8	0.00295	0.11943	>0.0264
					5.92	22.7	0.00461	0.18664	>0.0169
					8.53	20	0.00518	0.20972	>0.0117
KS2-2-4-6675.11 (Φ:5.28%; K:0.0081mD)	0.0007/ 0.0864	0.15	80.5	0.6667	0	100	0.00000	0.00000	–
					0.15	80.5	0.00004	0.00475	>0.6667
					0.46	77	0.00009	0.01096	>0.2174
					0.95	65	0.00072	0.08877	>0.1053
					2.13	47.6	0.00123	0.15185	>0.0470
					3.79	40.9	0.00131	0.16173	>0.0264
					5.92	22.7	0.00159	0.19630	>0.0169
					8.53	19.3	0.00168	0.20741	>0.0117
KS2-2-8- 6722.86 (Φ:5.97%; K:0.017mD)	0.0017/0.1	0.15	84.5	0.6667	0	100	0.00000	0.00000	–
					0.15	84.5	0.00007	0.00385	>0.6667
					0.46	64.5	0.00135	0.07941	>0.2174
					0.95	43.8	0.00412	0.24235	>0.1053
					2.13	33	0.00551	0.32412	>0.0470
					3.79	28.4	0.00615	0.36176	>0.0264
					5.92	15.9	0.00860	0.50588	>0.0169
					8.53	13.5	0.00916	0.53882	>0.0117

*S_{bc} is the water saturation when gas enters the pore space under displacement pressure.

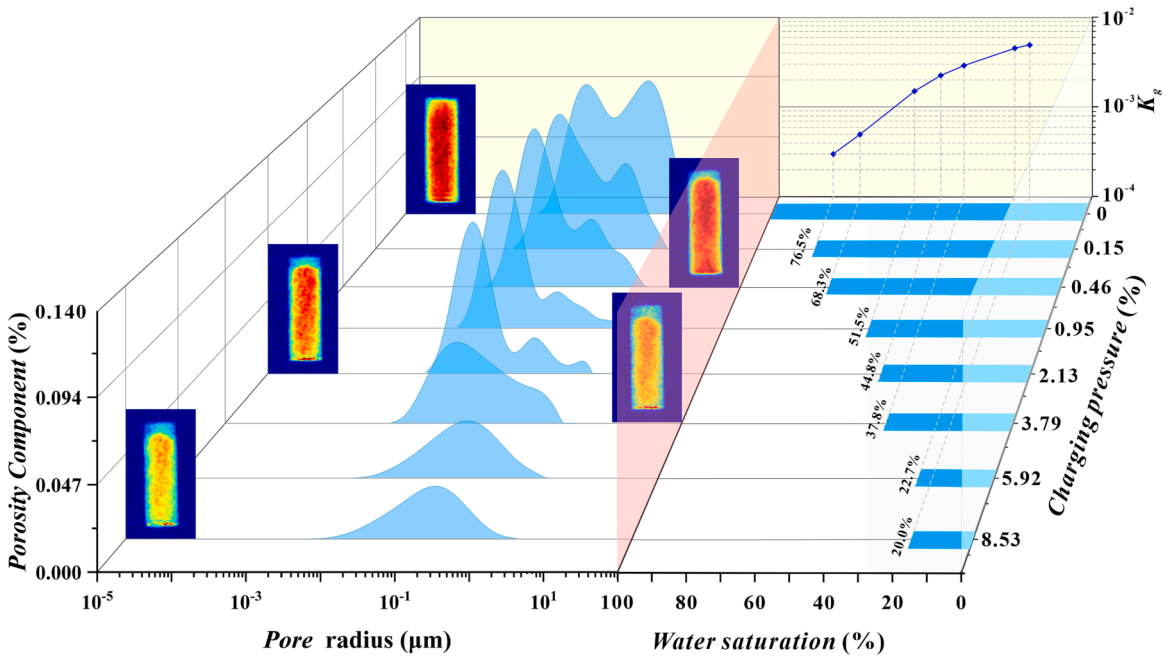

Fig. 7. Schematic diagram showing how PSD, water saturation, and relative gas permeability change during online gas-charging experiments (K208-6601.65).

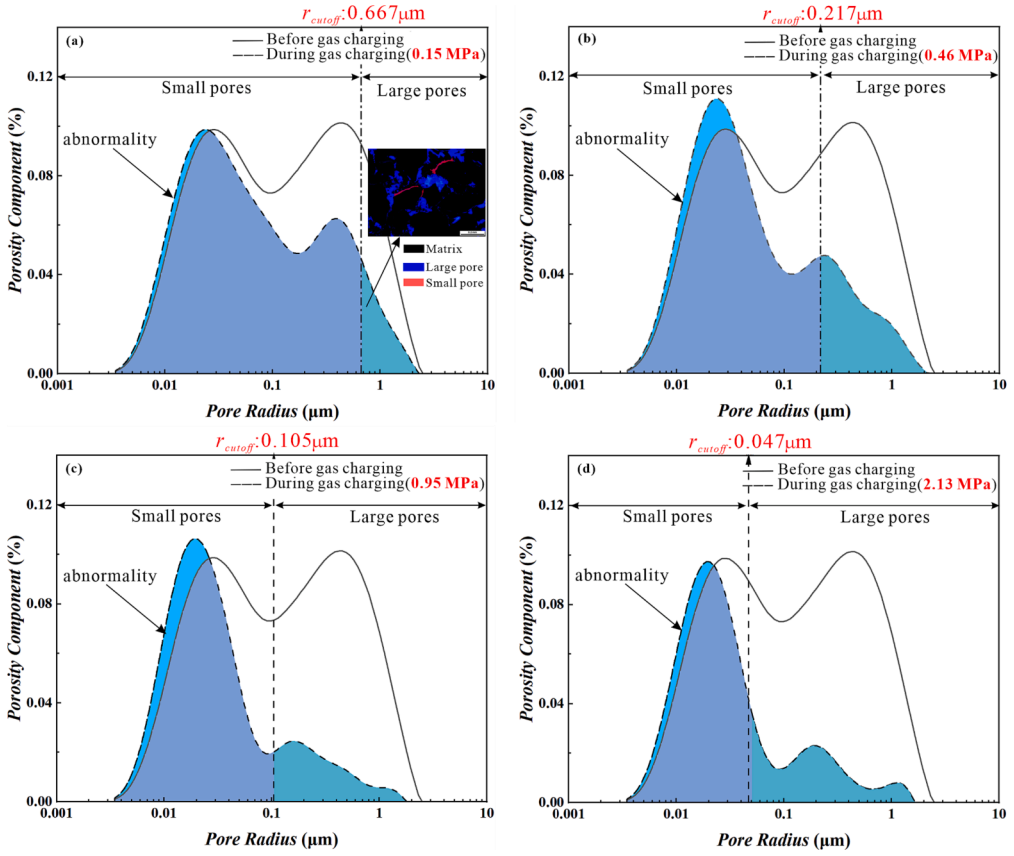

Fig. 8. The evolution of NMR PSDs during the gas-charging experiment under gradually increasing charging forces. (From 0.15 MPa to 2.13 MPa, K208-6601.65).

5.1.2. Water-film thickness and bound water saturation variation during the charging experiment

Based on the Derjaguin-Landau-Verwey-Overbee(DLVO) theory, we clarified the evolution of water-film thickness during the gas-charging process. (1) The water-film thickness fluctuated throughout the entire gas-charging experiment. (2) For pores of a certain radius, the thickness of the water-film in it reaches its maximum value when the charging force first surpasses its capillary force (gas starts to enter the pore space). The maximum water-film thickness of pores with different radii ranges from 0.36 to 9.34 nm (Fig. 9-a). (3) As the charging force increases, the

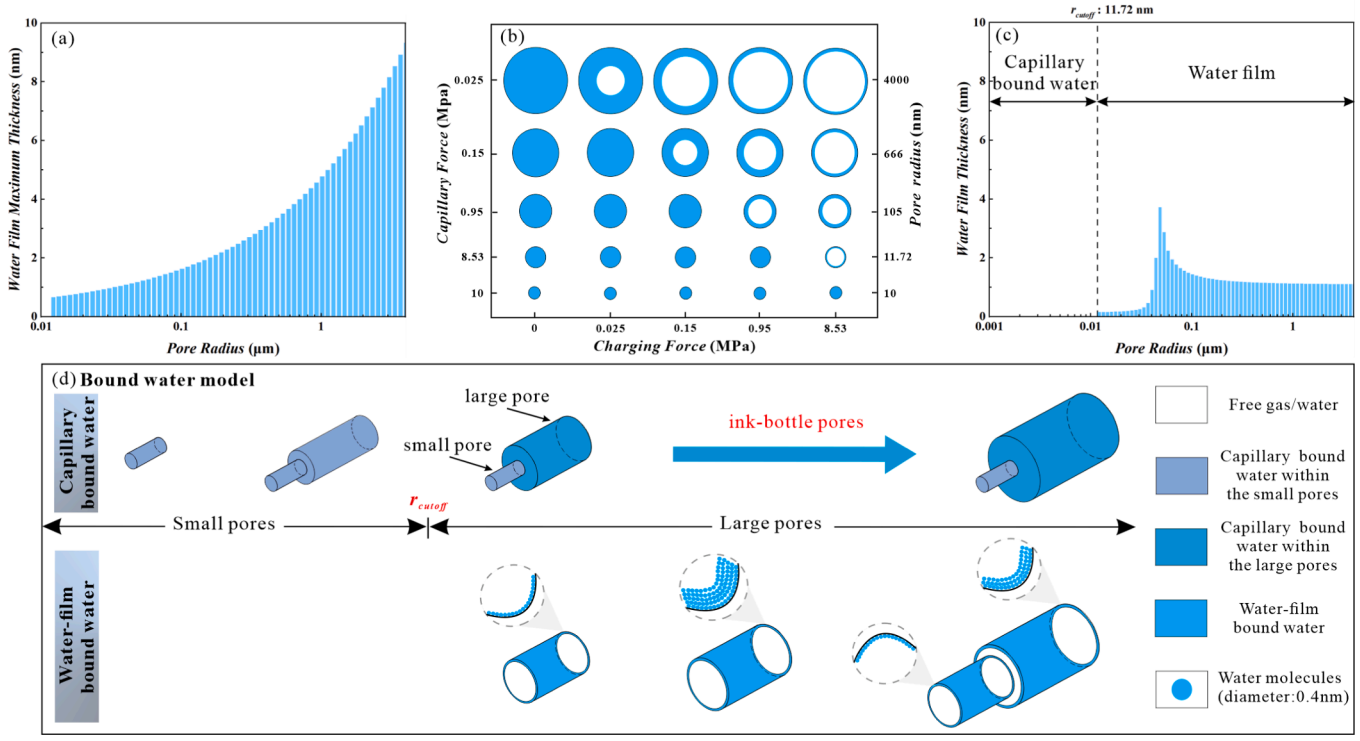

(a) The maximum water-film thickness (the charging force just exceeds the capillary force) of pores with different radii; (b) Schematic diagram of the evolution of water-film thickness in pores with different radii during the gas-charging experiment; (c) The minimum water-film thickness (when the charging force is 8.53 MPa) of pores with different radii; (d) A novel bound-water occurrence model.

Fig. 9. The evolution of water-film thickness during the gas-charging experiment and the bound water occurrence model.

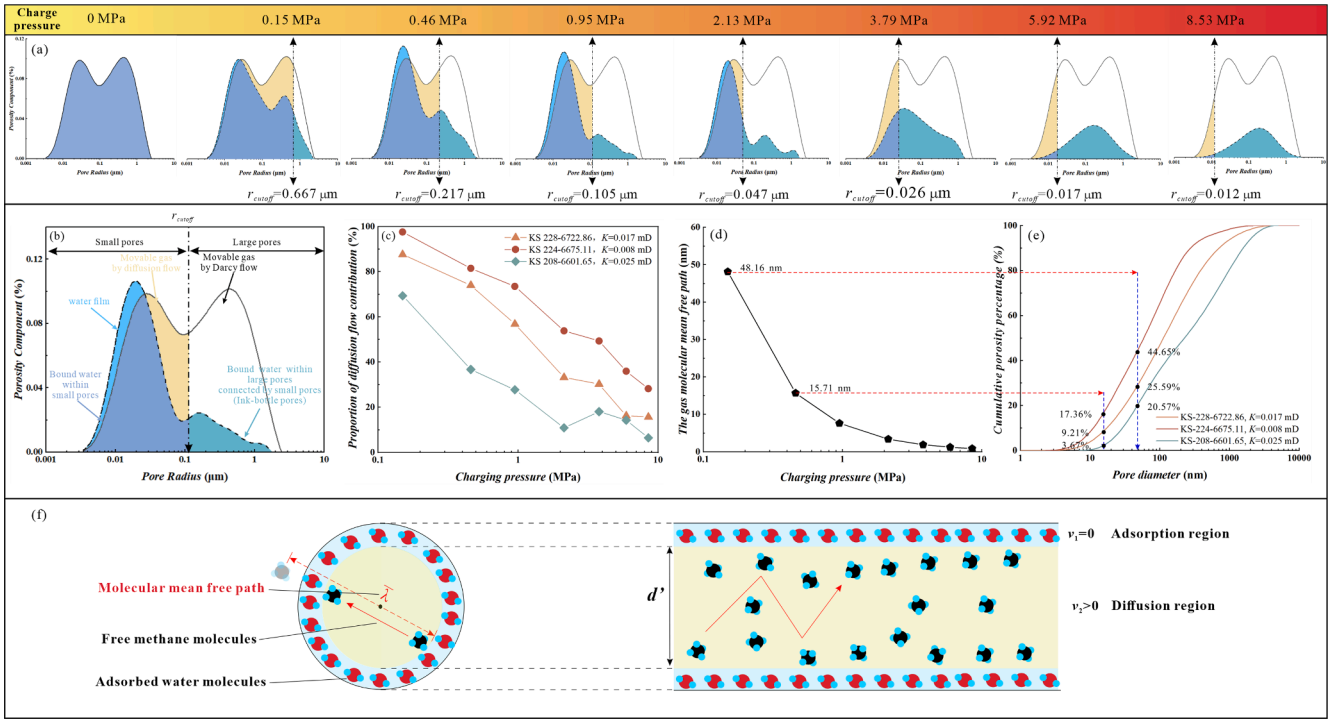

Fig. 10. The existence of the diffusion flow and its calculation.

water-film thickness gradually reduces (Fig. 9-b). The water-film thickness attains its minimum value upon reaching the maximum charging-force of 8.53 MPa. The minimum water-film thickness of pores with different radii ranges from 0.10 to 3.72 nm, and an increase in pore size resulted in an initial increase and subsequent decrease in water-film thickness, as depicted in Fig. 9-c. (4) It is noteworthy that the variation in thickness during the gas-charging experiment was minimal, ranging from 0.08 to 8.23 nm, and not statistically significant. (5) Upon completion of the gas charging process, the water-film saturations of the three tight sandstone samples ranged from 1.01% to 3.10%, with an average of 1.78%(Table 4 S_f), accounting for 1.75% to 22.96% of the total bound water saturation, with an average of 7.28%(Table 4 S_f / S_b). Thus, the water-film shows a widespread presence but low overall content—the bound water primarily consists of capillary-bound water.

In light of the research mentioned above, this study correlated the occurrence of bound water with hydrocarbon charging process and presented a novel bound water model (Fig. 9d) to comprehensively elucidate the presence of bound water in tight sandstone pore space: (1) The bound water comprises two components, namely capillary-bound water (within small pores and large pores restricted by small pores (ink-bottle pore)), and layered water-film within large pores as a consequence of electrochemical forces. (2) The lower limit of the large pores is subject to variation contingent upon the force exerted by hydrocarbon charging. (3) The water-film thickness in large pores is non-uniform, which can extend to encompass several water molecules. Additionally, the adsorption force between the water-film and the pore wall progressively strengthens from the outermost layer to the innermost layer. (4) The predominant type of bound water is capillary-bound water, with a relatively low content of water-film.

5.2. The influence of water-film on gas-charging lower limit and gas-flowing

The minimum pore/throat radius for gas-charging is crucial in hydrocarbon accumulation [52]. According to the Washburn Equation, the maximum gas-charging force in the online gas-charging experiment, determined to be 8.53 MPa, corresponds to a pore/throat radius of 11.72 nm. One debate regarding the lower pore/throat limit for gas-charge is: Is taking this value directly as the minimum gas-charging pore/throat radius rational? Considering the presence of a water-film with a thickness of 0.7 nm under this pressure, the minimum pore/throat radius for gas charging of the Bashijiqike tight sandstone should be adjusted to 12.42 nm. Overall, we believe that the influence of the water-film on the minimum pore/throat radius for gas charging in tight sandstone is deemed negligible.

To further investigate the influence of water-film on gas-flowing, we selected two samples that have undergone the NMR-supervised gas-charging experiment and conducted a mercury intrusion experiment. The Bashijiqike tight sandstone samples exhibit a maximum mercury injection saturation of nearly 100% (ranging from 98.67% to 100%, with an average of 99.34%). Therefore, integrating physical testing and mercury injection experiments enables the quantification of the permeability contribution from pores of varying sizes. For comparison's sake, we calculated the permeability contribution of pores with a radius between 0.1053 μm and 0.6667 μm (the decisive pore size range for seepage capacity, indicated by the NMR-gas-charging experiment), which ranges from 65.54% to 98.29% (with an average of 81.92%). This finding underscores the pivotal role played by pores within the aforementioned radius range in determining reservoir permeability. We compared the permeability obtained by the integration of the physical test and mercury intrusion experiment and that by the NMR online gas-charging experiment: the permeability (K_{ag}, Table 5) under single-phase conditions is significantly higher than the effective gas permeability (K_g, Table 5) during the gas-charging experiment. Specifically, the latter is 46.11%–97.84% lower than the former (Table 5, last column), with an average reduction of 78.37%. In gas-charging, gas gradually "pulls" water out of the pore space. The pore space that gas did not flood is saturated with formation water, while the gas-existing pore space contains only gas and water-film. Thus, the reduction in permeability in the same pore size range is due to the existence of water-film. To conclude, a water-film substantially influences gas-flowing (Table 5).

From the perspective of mass flux in nanopores, gas percolation can be characterized by Diffusion, Slip, and Darcy flow. Previous beliefs suggested that in tight rocks, the slippage effect deviates the gas flow in nanoscale pores from adhering to Darcy's law [27,53]. However, these beliefs are primarily derived from studies on single-phase seepage in porous media. In reality, tight gas reservoirs often exhibit gas-water two-phase seepage. The preferential adsorption of water molecules on the pore surface forms a sandwich structure consisting of a water-film, gas, and another water-film within the pores[30]. A water-film in nanoscale pores creates a shielding effect that prevents gas from slipping when a two-phase seepage of water and gas occurs. As a result, gas flow adheres

Table 4
Parameters for the calculation of water-film thickness and saturation.

Samples	V cm^3	V_p cm^3	V_f cm^3	V_b cm^3	S_f %	S_{cw} %	S_f / S_b %	S_{cw} / S_b %
KS 208-6597.15	18.66	1.1924	0.0219	0.3324	1.83	26.05	6.58	93.42
KS208-6601.65	15.94	1.0227	0.0171	0.1896	1.67	16.87	9.00	91.00
KS 208-6602.06	19.30	1.0712	0.0109	0.4672	1.02	42.60	2.33	97.67
KS 208-6602.52	16.70	0.7181	0.0105	0.2673	1.46	35.76	3.92	96.08
KS 208-6609.78	17.02	0.7812	0.0106	0.3968	1.35	49.44	2.66	97.34
KS 208-6610.17	18.14	0.8834	0.0131	0.4457	1.48	48.97	2.93	97.07
KS 224-6674.13	19.67	0.8596	0.0180	0.2529	2.09	27.33	7.12	92.88
KS 224-6675.11	16.25	0.8575	0.0225	0.1655	2.63	16.67	13.62	86.38
KS 224-6687.45	17.63	0.8462	0.0169	0.1617	2.00	17.11	10.46	89.54
KS 224-6691.93	16.43	0.6802	0.0133	0.1805	1.96	24.57	7.37	92.63
KS 228-6709.26	15.70	0.6924	0.0120	0.1482	1.74	19.66	8.11	91.89
KS 215-6714.71	19.25	1.1011	0.0145	0.4161	1.31	36.48	3.48	96.52
KS 215-6725.44	18.94	1.1299	0.0159	0.2999	1.41	25.13	5.31	94.69
KS 228-6722.86	19.03	0.9458	0.0293	0.1277	3.10	10.40	22.96	77.04
KS 215-6730.6	19.88	1.1252	0.0210	0.1911	1.87	15.11	11.00	89.00
KS 215-6730.77	19.42	1.0429	0.0186	0.2215	1.79	19.45	8.41	91.59
KS 215-6738.04	16.36	0.8180	0.0198	0.2812	2.43	31.95	7.06	92.94
KS 215-6740.3	18.40	1.0138	0.0210	0.2810	2.07	25.65	7.46	92.54
KS 215-6741.77	17.62	0.8246	0.0127	0.3472	1.54	40.57	3.65	96.35
KS 225-6775.48	17.80	0.8704	0.0134	0.3345	1.54	36.89	4.00	96.00
KS 225-6776.75	21.44	1.5973	0.0321	0.2770	2.01	15.33	11.58	88.42
KS 223-6805.63	19.36	1.2971	0.0217	0.3223	1.67	23.18	6.73	93.27
KS 207-6867.85	17.71	0.7314	0.0074	0.4237	1.01	56.92	1.75	98.25

Table 5
Parameters related to gas permeability in different pore spaces.

Samples	Pore Space μm	Permeability contribution (cumulative) %		K_{ag} mD	K_g mD	Permeability reduction %
KS208-6601.65 (Φ:6.42%;K:0.0247mD)	>0.6667	33.19	**65.54%** (from 0.1053 to 0.6667 μm)	0.0082	0.0003	96.3405
	>0.2174	93.63		0.0231	0.0005	97.8380
	>0.1053	98.73		0.0244	0.0016	93.4389
	>0.0470	99.66		0.0246	0.0022	90.9002
	>0.0264	99.91		0.0247	0.0030	88.0459
	>0.0169	99.96		0.0247	0.0046	81.3286
	>0.0117	99.98		0.0247	0.0052	79.0241
KS2-2-8- 6722.86 (Φ:5.97%;K:0.017mD)	>0.6667	0.00	**98.29%** (from 0.1053 to 0.6667 μm)	0.0000	0.0001	–
	>0.2174	77.58		0.0132	0.0014	89.7639
	>0.1053	98.29		0.0167	0.0041	75.3431
	>0.0470	99.70		0.0169	0.0055	67.4907
	>0.0264	99.92		0.0170	0.0062	63.7946
	>0.0169	99.97		0.0170	0.0086	49.3966
	>0.0117	99.99		0.0170	0.0092	46.1123

*K_{ag}: the permeability calculated by integrating physical test and mercury intrusion experiment, single-phase permeability;
*K_g: the permeability calculated from the NMR-supervised gas-charging experiment, gas-water two-phase.

to Darcy's law [29,30] and is primarily governed by Darcy flow and diffusion flow[54]—the primary mechanisms for gas-flowing in reservoirs [55].

Darcy flow refers to the movement of natural gas in the porous medium driven by pressure differences. Accordingly, Darcy flow only transpires in the pore space with a pore size larger than r_{cutoff}, where the charging force surpasses the corresponding capillary pressure [56]. Nevertheless, NMR PSD from the online gas-charging experiment reveals the existence of a substantial quantity of movable water in smaller (than r_{cutoff}) pores (Fig. 10a-b yellow-colored). This inconsistency confirms the existence of diffusion flow: under the influence of a concentration gradient, free gas diffuses from the high-concentration area (large pores) to the low-concentration area (small pores) [57].

It is evident that the three samples exhibit similar changing patterns (Fig. 10 c)—the contribution of diffusion flow diminishes with increasing charging pressure. When the diffusion flow controlled 50% of the movable fluid, the corresponding charging pressure for samples KS 228–6722.86, KS 224–6675.11, and KS 208–6601.65 were measured at 1.28, 3.53, and 0.32 MPa, respectively, with an average of 1.71 MPa. Hence, in the case of low pressure (<1.71 MPa), gas migration in tight sandstone is primarily governed by diffusion flow, followed by Darcy flow. However, when in a high-pressure range, the dominant form of gas seepage is Darcy flow, adhering to Darcy's law, and diffusion manifestation becomes less pronounced. This phenomenon can be attributed to the rise in pressure and the reduction in the average free path of gas molecules, resulting in an increased proportion of pores with pore throat radius surpassing the molecular mean free path(Fig. 10d and f, Equation (15). Consequently, this unfavorable condition impedes diffusion flow. Furthermore, the proportion of diffusion flow increases as the sample's permeability decreases (Fig. 10e). This suggests that diffusion flow is more pronounced in samples with lower permeability. This phenomenon can be attributed to the fact that samples with lower permeability tend to have a higher proportion of pores smaller than the molecular mean free path, thereby facilitating diffusion flow.

$$\bar{\lambda} = \frac{KT}{\sqrt{2}\pi d^2 p} \tag{15}$$

where $\bar{\lambda}$ is the mean free path of the gas molecules, m; K is the Boltzmann constant, 1.3805×10^{-23} J·K^{-1}; T is the temperature, K; d is the collision diameter of the gas molecules, m, here $d = 0.36 \times 10^{-9}$ m; p is pressure, Pa.

5.3. Influencing factors on bound water saturation

To comprehensively analyze the potential influencing factors on bound water saturation, we first analyzed relationships between the bound water saturation and reservoir parameters from macroscopic to microscopic, including physical properties, pore structure parameters, mineral compositions, and fractal dimension. Based on it, the grey relation analysis was used to explore the complex nonlinear relationships between bound water saturation and different parameters to clarify the utmost critical factor.

5.3.1. The relationships between bound water saturation and petrophysical properties

Bound water saturation is an essential parameter in reservoir evaluation [32]. There is often a good negative correlation between the physical properties of conventional reservoirs and bound water saturation [11,31]. However, due to the robust reservoir heterogeneity of Bashijiqike tight sandstone, there is no relationship between bound water saturation and permeability (Fig. 11 b) and a weak negative correlation with porosity (Fig. 11 a). The limited correlation between porosity and bound water saturation may be attributed to the "ink-bottle" pore structure (Fig. 8 a), which hinders the fluid's mobility within larger pores, diminishing the correlation between porosity and movable fluid. The greater the complexity of the pore structure, particularly the prevalence of the "ink bottle" pore structure, the more pronounced the restriction on bound water saturation [58]. The absence of a correlation between permeability and bound water saturation may be attributed to pore spaces with an equivalent radius exceeding 0.1 μm (Table 5) contributing over 98% of reservoir permeability. Conversely, bound water primarily accumulates within pores with a radius smaller than 0.1 μm, rendering changes in bound water content minimally impactful on permeability(Table 5).

5.3.2. The relationships between pore structure parameters and bound water saturation

The PSD mainly controls bound water saturation within the reservoir rocks [4]. The NMR PSD (Fig. 10 a) demonstrates that when subjected to a charging force of 8.53 MPa, bound water predominantly resides within small pores measuring less than 11.72 nm in radius, as well as the larger pores interconnected with them (Table 4, S_{cw} / S_b:77.04 %-98.25%, average 92.72%). However, we found a relatively poor positive correlation between bound water saturation and the proportion of pores smaller than 11.72 nm (R^2 = 0.24, Fig. 12a). Therefore, bound water saturation in tight reservoirs is not simply controlled by the proportion of small pores. In contrast, the positive correlation between bound water saturation and "ink-bottle" pores proportion (R^2 = 0.47, Fig. 12b) is more prominent than the former. It demonstrates that bound water remaining in the pore space is predominantly stored in the large pores (31.03%-97.06%, average 66.81%) restricted by pores smaller than 11.72 nm. Thus, the "ink-bottle" pore structure significantly affects

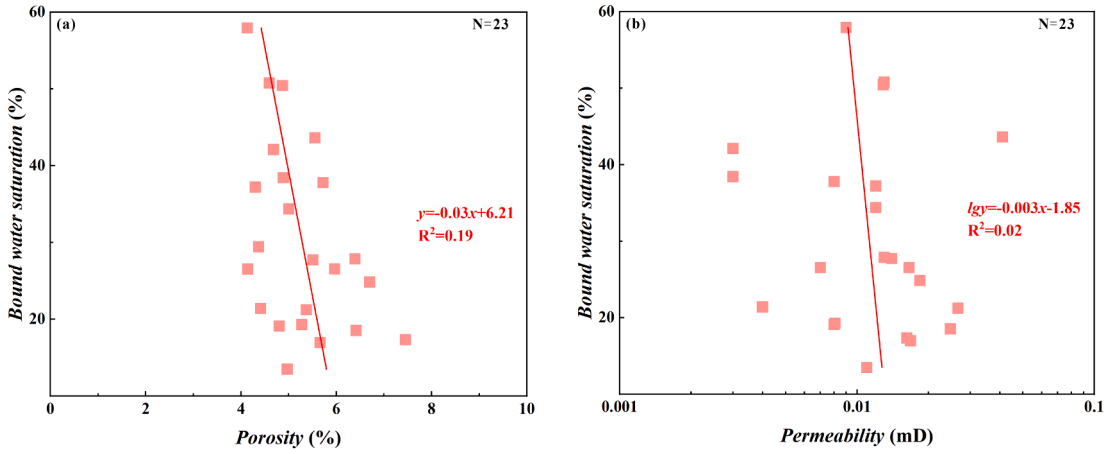

(a) Cross-plot of bound water saturation versus porosity; (b) Cross-plot of bound water saturation versus permeability.

Fig. 11. Relationship between petrophysical properties and bound water saturation.

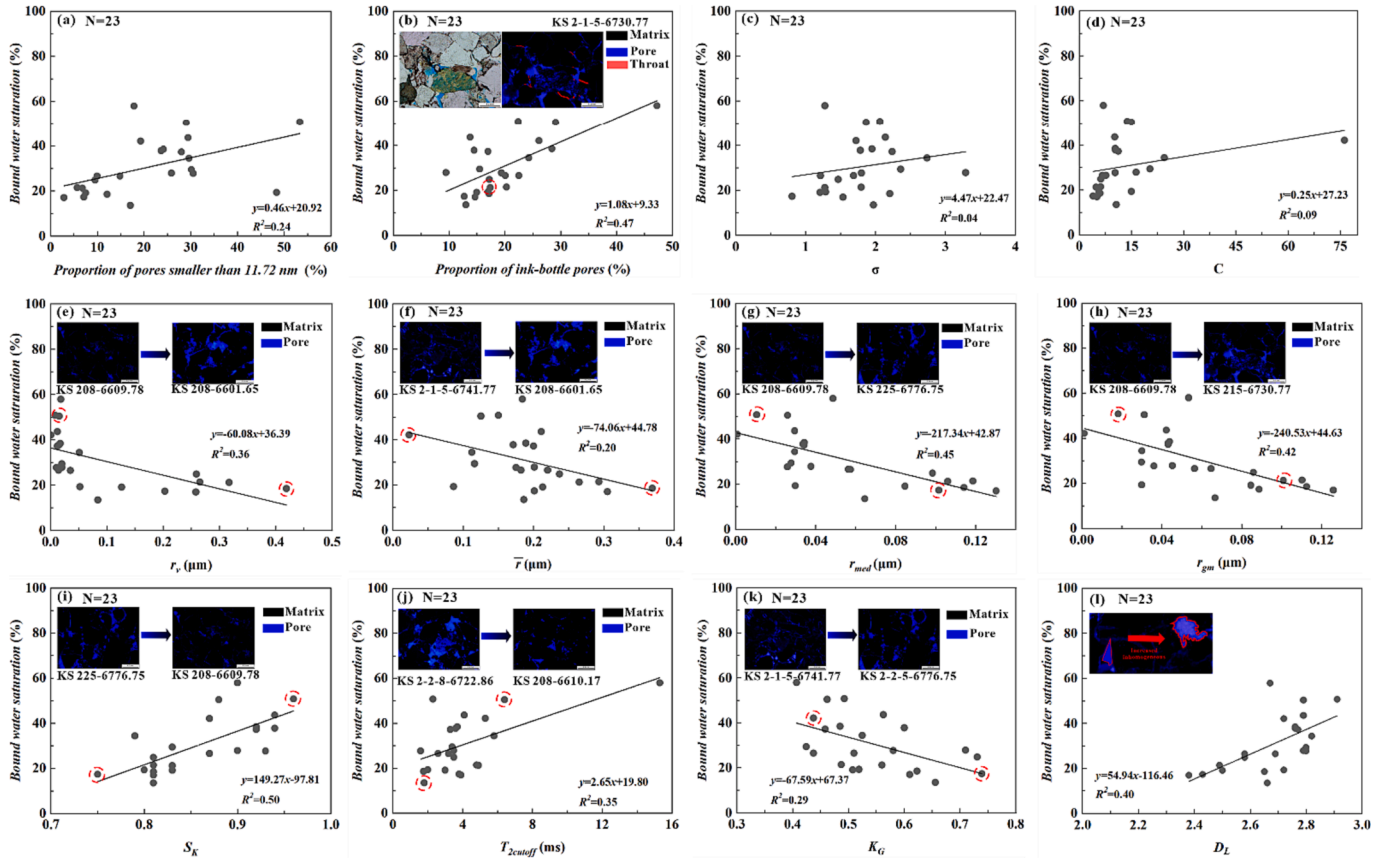

Fig. 12. Relationships between pore structure parameters and bound water saturation.

bound water saturation [36,37]. The more large pore space the "ink-bottle" pore structure restricts, the higher the bound water saturation.

Moreover, we examined the correlation relationships between the bound water saturation and several pore structure parameters derived from NMR and fractal analysis (Table 1). The results show that among the ten parameters, only σ (sorting coefficient) and C (coefficient of variation) have no correlation relationship with bound water saturation at all (Fig. 12 g-k).

r_v (the peak value of PSD), $\bar{r}$ (the average pore size), r_{med} (the median pore size) and r_{gm} (the geometric mean pore radius) negatively correlate with bound water saturation (R^2 is 0.36, 0.20, 0.45, and 0.42, respectively), indicating that the smaller the overall pore size, the greater the bound water saturation. It is worth noting that r_{med} and r_{gm} have a better correlation relationships with bound water saturation than r_v and $\bar{r}$. Thus, we recommend to utilize median and geometric mean pore size than average in predicting bound water saturation for tight sandstone. r_{med} and r_{gm} are more representative values that can better describe pore structure heterogeneity. S_k (Skewness), T_{cutoff} positively correlates with bound water saturation (R^2 is 0.50 and 0.35, respectively). The positive S_k value means a right-skewed pore size distribution—small pores

dominate the pore space. The higher the S_k, the smaller the overall pore size and the higher the bound water saturation. $T_{2cutoff}$ is the partition value (a relaxation time threshold) in centrifugation-coupled NMR test to determine movable and immovable (bound) fluids: the higher the $T_{2cutoff}$, the higher bound water saturation [59]. Thus, there is a positive correlation between $T_{2cutoff}$ and bound water saturation. However, we found that their positive correlation relationship is relatively weak—the validity of the empirical way to obtain $T_{2cutoff}$ fluctuates in tight sandstone research [60]. It also infers that using the $T_{2cutoff}$ as a critical parameter for predicting bound water saturation may be questionable.

Additionally, K_G (kurtosis) negatively correlates with bound water saturation ($R^2 = 0.29$): higher K_G values correspond to a more concentrated PSD, reduced variation in pore size within the pore space, and a decreased likelihood of ink-bottle pore formation, ultimately resulting in lower bound water saturation.

The fractal dimension within the range of large pores (D_L) positively correlates with bound water saturation($R^2 = 0.40$). This can be attributed to two aspects. Firstly, an increase in the fractal dimension of large pores results in a rougher inner surface [61], thereby enhancing the adsorption area and facilitating the formation of a water-film [62]. Secondly, a higher fractal dimension implies a more intricate structure of the large pores and poorer connectivity, thereby increasing the likelihood of connectivity with small pores to form an ink-bottle pore structure [63].

5.3.3. *Effect of mineral compositions on bound water saturation*

The Bashijiqike tight sandstone in the study area has experienced substantial compaction due to burial depth and multiple tectonic movements [64]. Both quartz and feldspar demonstrate considerable resistance to compaction (small figure in Fig. 13 a and b), thereby providing stability to the rock framework [65]. Therefore, a higher proportion of quartz and feldspar usually results in increased pore space for movable fluid—the content of quartz and feldspar should exhibit a negative correlation with bound water saturation [66]. In the study area, the quartz content displays a negative correlation with bound water saturation (Fig. 13a), whereas feldspar does not (Fig. 13b). This phenomenon may be because feldspar acts as a source for clay precipitation through its dissolution(Fig. 13b little figure) [67], which leads to the obstruction of intergranular pores surrounding the feldspar by authigenic clay minerals, generating micropores—the bound water saturation increases [68].

Moreover, we analyzed the relationships between clay minerals and the bound water saturation. In this process, certain outliers (the black circles in Fig. 13-c, e, and f) significantly impact the correlation analysis. When these points are considered, there is minimal correlation between bound water saturation and total clay content, I/S content, and illite content (with R^2 values of 0.09, 0.16, and 0.07, respectively). However, upon disregarding these outliers, a strong positive correlation emerges: R^2 is 0.61, 0.53, and 0.56, respectively. It demonstrates that the bound water saturation is significantly influenced by clay minerals, primarily by I/S-mixed layers and illite, but not chlorite (Fig. 13d).

Statistical parameters, such as Pearson's r and R^2, are commonly employed in the correlation analysis between two variables. However, these parameters solely capture the linear correlation between variables. A low linear correlation coefficient merely indicates the absence of a linear correlation, while the possibility of a nonlinear correlation remains. Additionally, it is crucial to consider the influence of outliers on linear correlation analysis, as demonstrated in previous research (Fig. 13-c, e, and f). Moreover, it is hard to determine the dominant factor controlling the bound water saturation based on linear correlation analysis.

Hence, we introduced Grey Relational Analysis (GRA) to comprehensively depict the correlation relationships among various parameters. Notably, the Grey Relation Analysis (GRA) does not necessitate data size and exhibits robustness against the impact of outliers, thereby ensuring the congruity between quantitative and qualitative analysis outcomes. A high grey relation degree (GRD) signifies a strong alignment in the changing trends of two variables, while a low GRD indicates

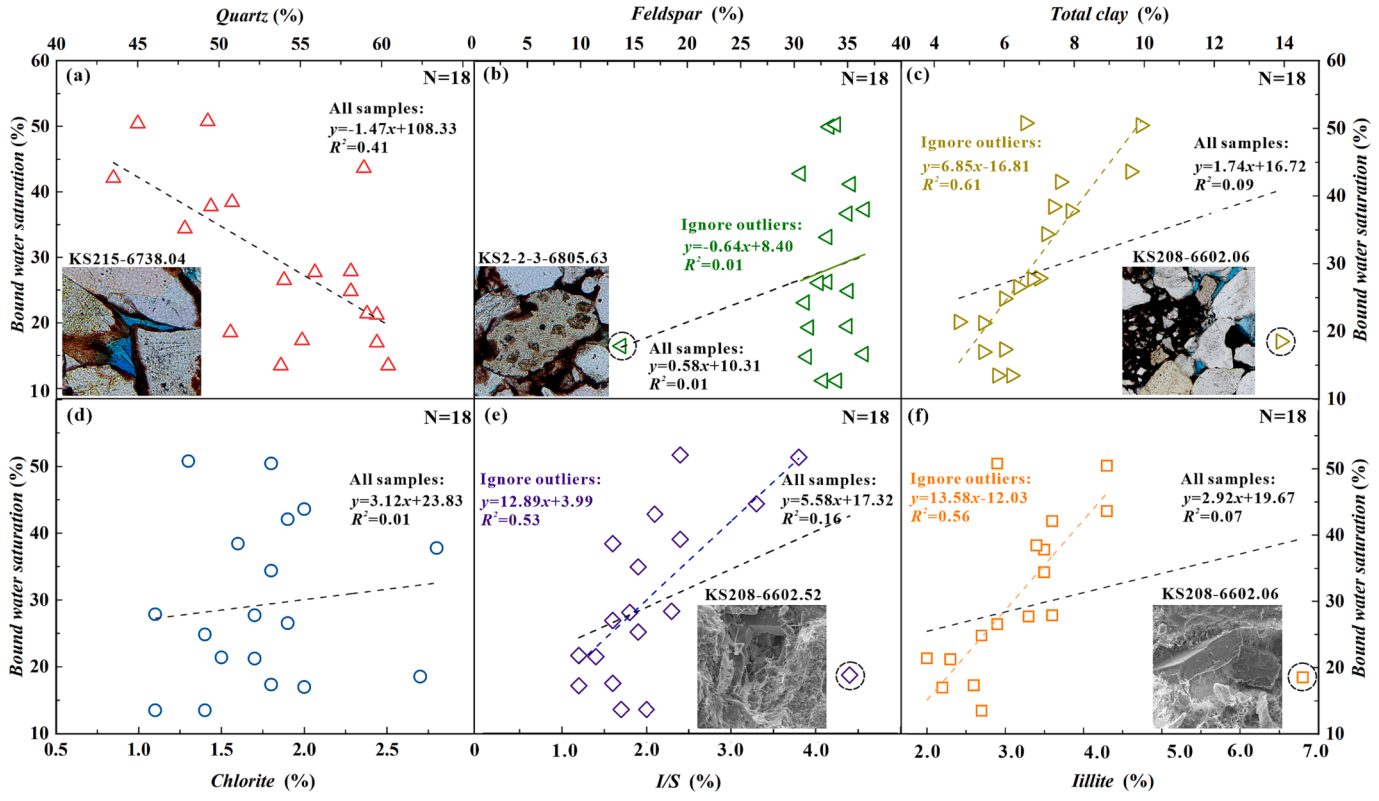

Fig. 13. Relationship between mineral content and bound water saturation.

inconsistency (Fig. 14a).

Clearly, the clay content, particularly the I/S and Illite content (Fig. 14b), significantly influences the bound water saturation, as indicated by a grey relation degree of 0.82, surpassing all other factors. This finding aligns with the correlation analysis presented in Fig. 13, disregarding outliers. The proposed bound water model suggests that it consists of capillary-bound water in small pores (and large pores restricted by small pores/throats) and water-film in large pores. The capillary-bound water is primarily influenced by the capillary force, which is determined by the pore structure, while the water-film is primarily influenced by the adhesion force. When fibrous, flaky, and curved illite is distributed in the pore space, especially within intergranular pores or on the surface of grains (small figurre in Fig. 13 e), the original large intergranular pores will be segmented into small ones[69]. Similarly, Abitkazy (2021) [70] also reported that the illite/smectite occurring in silk-, strip- or bridge-like forms extend from the surface of the mineral grains and intersect pore spaces (small figurre in Fig. 13 f), leading to increased small pores and more complicated pore/throat system. In our study, Grey Relational Analysis further verifies that the I/S-mixed layer and illite exert the most significant influence on the formation of small pores (with GRD of 0.75 and 0.73, respectively) and ink-bottle pores (with GRD of 0.79 and 0.84, respectively).

To summarize, an augmentation in the I/S-mixed layer and illite composition will engender a greater abundance of small pores and ink-bottle pores, consequently leading to an escalation in capillary-bound water and ultimately resulting in an augmented bound water content. Last but not least, illite and I/S-mixed layer are characterized by high surface area and CEC (cation exchange capacity), resulting in high water adsorption capacity. Therefore, thin layers of illite or I/S-mixed layer coating the grain surface (large pores surface) further contribute to the augmentation of water-film content. However, this is not the leading cause compared to capillary-bound water.

6. Conclusions

In this study, we correlated the occurrence of bound water with the hydrocarbon charging process and introduced a new parameter, r_{cutoff}, which is subject to variation contingent upon the force exerted by hydrocarbon charging. We presented a novel bound water model to comprehensively elucidate the occurrence of bound water in tight sandstone pore space. The bound water comprises two components: capillary-bound water within small pores ($<r_{cutoff}$) and restricted (by pore/throat $< r_{cutoff}$) large pores, layered water-film within large pores ($>r_{cutoff}$) formed by electrochemical forces. The water-film thickness is non-uniform, which can extend to encompass several water molecules. Additionally, the adsorption force between the water-film and the pore wall progressively strengthens from the outermost layer to the innermost layer. The predominant type of bound water is capillary bound water, with a relatively low content of water-film.

Water-film has a negligible impact on the lower threshold of gas-charging (0.7 nm), rendering it inconsequential. However, the presence of a water-film significantly alters the physical characteristics of the reservoir, resulting in a reduction in gas permeability ranging from 46.11% to 97.84% (with an average reduction of 78.37%). Moreover, water-film alters the gas seepage mechanism, eliminating the slip effect and leaving only Darcy and Diffusion flow as dominant types. Furthermore, in the low-pressure range, gas migration in tight sandstone is primarily governed by diffusion flow, followed by Darcy flow. However, in the high-pressure range, the dominant form of gas seepage is Darcy flow, adhering to Darcy's law, and diffusion behavior manifestation becomes less pronounced.

I/S-mixed layer and illite exert the most significant influence on bound water saturation: an augmentation in the I/S-mixed layer and illite composition will engender a greater abundance of small pores and ink-bottle pores, consequently leading to an escalation in capillary-bound water and ultimately resulting in an augmented bound water content.

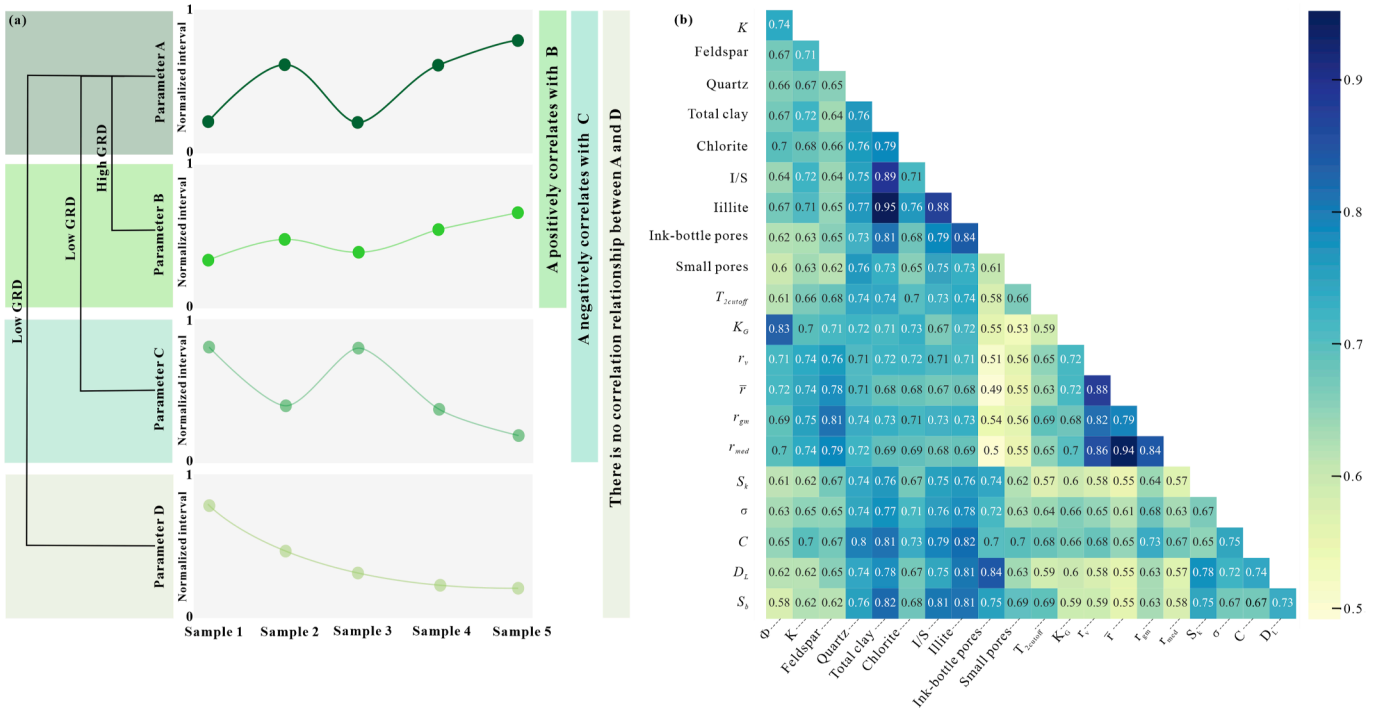

(a) Schematic diagram of Grey Relational Analysis (GRA); (b) Heat map showing the the grey relation degree (GRD) between variables.

Fig. 14. Grey Relational Analysis on the controlling factor on bound water saturation.

CRediT authorship contribution statement

Zezhang Song: Supervision, Investigation, Writing – review & editing. **Lv Mingyang:** Methodology, Investigation, Writing – original draft, Data curation. **Zhao Libin:** Project administration, Resources. **Liu Changqi:** Investigation, Data curation. **He Yuanyuan:** Project administration, Resources. **Zhang Yueqiao:** Project administration, Resources. **M.A. Lobusev:** Methodology.

Declaration of Competing Interest

The authors declare the following financial interests/personal relationships which may be considered as potential competing interests: Song Zezhang reports financial support was provided by PetroChina-Research Institute of Petroleum Exploration and Development, National Natural Science Foundation of China, and Petrochina Tarim Oilfield Company.

Data availability

Data will be made available on request.

Acknowledgments

This research was financially sponsored by CNPC Innovation Fund (Grant No. 2021DQ02-0105), General Program of National Natural Science Foundation of China (Grant No. 42272161), the 14th Five-Year Plan's Forward-looking and Basic Major Scientific Research Project - Research on the hydrocarbon enrichment law in lithologic reservoirs and the evaluation technology of favorable zones (2021DJ0404), Research and field application of technologies for efficient development of complex oil and gas reservoirs in Bozi-Dabai trillion-cubic-meter-scaled gas area (NO. TXN011020120001) and the State Key Laboratory of Petroleum Resources and Prospecting (Grant No. 2462023BJRC023, 2462017YJRC025, Grant No. PRP/indep-04-1611). We would also like to thank PetroChina Tarim Oilfield Company for providing core samples and necessary data.

References

[1] Wu XZ, Liuzhuang XX, Wang J, Zheng M, Chen XM, Qi XF. Petroleum Resource Potential, Distribution and Key Explorationfields in China. Earth Sci Front 2022;29(6):146–55.
[2] Dai J, Ni Y, Wu X. Tight Gas in China and its Significance in Exploration and Exploitation. Pet Explor Dev 2012;39(3):277–84.
[3] Jin G, Xie R, Xiao L, Wu B, Xu C, Wang X, et al. Quantitative Characterization of Bound and Movable Fluid Microdistribution in Porous Rocks Using Nuclear Magnetic Resonance. J Pet Sci Eng 2021;196:107677.
[4] Lai FP, Li ZP, Zhang W, Dong HK, Kong FS, Jiang ZY. Investigation of Pore Characteristics and Irreducible Water Saturation of Tight Reservoir Using Experimental and Theoretical Methods. Energy Fuel 2018;32(3):3368–79.
[5] Zhang F, Jiang Z, Sun W, Li Y, Zhang X, Zhu L, et al. A Multiscale Comprehensive Study on Pore Structure of Tight Sandstone Reservoir Realized by Nuclear Magnetic Resonance, High Pressure Mercury Injection and Constant-Rate Mercury Injection Penetration Test. Mar Pet Geol 2019;109:208–22.
[6] Jiang M, Fang H, Liu Y, Zhang Y, Wang C. On Movable Fluid Saturation of Tight Sandstone and Main Controlling Factors -Case Study on the Fuyu Oil Layer in the Da'an Oilfield in the Songliao Basin. Energy 2023;267:126476.
[7] Xie Z, Yang C, Li J, Zhang L, Guo J, Jin H, et al. Accumulation Characteristics and Large-Medium Gas Reservoir-Forming Mechanism of Tight Sandstone Gas Reservoir in Sichuan Basin, China: Case Study of the Upper Triassic Xujiahe Formation Gas Reservoir. J Nat Gas Geosci 2021;6(5):269–78.
[8] Hoffman BT. Comparison of Various Gases for Enhanced Recovery from Shale Oil Reservoirs. SPE Improved Oil Recovery Symposium. 2012:SPE-154329-MS.
[9] He YD, Mao ZQ, Xiao LZ, Ren XJ. An Improved Method of Using NMR T-2 Distribution to Evaluate Pore Size Distribution. Chinese J Geophys-Chinese Edition 2005;48(2):373–8.
[10] Meng M, Ge H, Shen Y, Ji W, Wang Q. Rock Fabric of Tight Sandstone and its Influence on Irreducible Water Saturation in Eastern Ordos Basin. Energy Fuel 2023;37(5):3685–96.
[11] Dai Q, Luo Q, Zhang C, Lu C, Zhang Y, Lu S, et al. Pore Structure Characteristics of Tight-Oil Sandstone Reservoir Based on a New Parameter Measured by NMR Experiment:a Case Study of Seventh Member in Yanchang Formation. Ordos Basin Acta Petrolei Sinica 2016;37(7):887–97.
[12] Coates GR, Marschall D, Mardon D, Galford J. A New Characterization of Bulk-Volume Irreducible Using Magnetic Resonance. Log Analyst 1997;39(1):51–63.
[13] Messer ES. Interstitial Water Determination by an Evaporation Method. J Petrol Tech 1951;3(10):269–74.
[14] Martin P, Dacy J. Effective Qv By Nmr Core Tests. SPWLA 45th Annual Logging Symposium. 2004:SPWLA-2004-HH.
[15] Yang ZQ, Tang XL, Xiao HM, Zhang F, Jiang ZX, Liu G. Water Film Thickness of Tight Reservoir in Fuyu Oil Layer of Cretaceous Quantou Formation in Songliao Basin and its Influence on the Lower Limit of Seepage. Mar Pet Geol 2022;139:105592.
[16] Saidi A, Melrose JC. Discussion of Valid Capillary Pressure Data at Low Wetting-Phase Saturation. Reply 1991.
[17] Zhang H, Zhong Y, She JP, Li GF. Characterization of Shale Matrix Pore Structure via Experiment and Model. Arab J Geosci 2018;11(12).
[18] Wang WM, Lu SF, Tian WC, Zhou NW, Li JJ, Shan JF, et al. A New Method to Determine Porosity and Permeability Cutoffs of Tight Oil Reservoirs by Using Thickness of Adsorption Water Film: a Case Study from the Damintun Sag. Liaohe Oifield Oil&Gas Geol 2016;37(01):135–40.
[19] Li J, Wang W, Lu S, Chen X, Fan T, Li J, et al. Using Thickness of Adsorption Water Film to Determine Lower Limits of Physical Parameters of Unconventional Gas Reservoir-Taking Turpan-Hami Basin as an Example. J Nanosci Nanotechnol 2017;17(9):6262–7.
[20] Xiao Q, Wang Z, Yang Z, Xiang Z, Liu Z, Yang W. Novel Method for Determining the Lower Producing Limits of Pore-Throat Radius and Permeability in Tight Oil Reservoirs. Energy Rep 2021;7:1651–6.
[21] Liu M, Xie R, Guo J, Jin G. Characterization of Pore Structures of Tight Sandstone Reservoirs by Multifractal Analysis of the NMR T2 Distribution. Energy Fuel 2018;32(12):12218–30.
[22] Liu Y, Yao Y, Liu D, Zheng S, Sun G, Chang Y. Shale Pore Size Classification: an NMR Fluid Typing Method. Mar Pet Geol 2018;96:591–601.
[23] Nabawy BS, Géraud Y, Rochette P, Bur N. Pore-Throat Characterization in Highly Porous and Permeable Sandstones. AAPG Bull 2009;93(6):719–39.
[24] Li X, Xu S, Hao Y, Li D, Lu D. Gas Transport in Shale Nanopores with Miscible Zone. Geofluids 2020;2020:6410614.
[25] Li T, Song H, Wang J, Wang Y, Killough J. An Analytical Method for Modeling and Analysis Gas-Water Relative Permeability in Nanoscale Pores with Interfacial Effects. Int J Coal Geol 2016;159:71–81.
[26] He M, Zhou Y, Wu K, Hu Y, Feng D, Zhang T, et al. Pore Network Modeling of Thin Water Film and its Influence on Relative Permeability Curves in Tight Formations. Fuel 2021;289:119828.
[27] Li Y, Li X, Shi J, Wang H, Wu L, Teng S. A Nano-Pore Scale Gas Flow Model for Shale Gas Reservoir. SPE Energy Resources Conference. Day 2 Tue, June 10, 2014. 2014.
[28] Wang M, Yu Q. Comparing the Permeability of Dry and Moisturized Crushed Shales Determined by the Dynamic Process Data of Methane Adsorption. J Hydrol 2020;590:125375.
[29] Liu B, Qi C, Zhao X, Teng G, Zhao L, Zheng H, et al. Nanoscale Two-Phase Flow of Methane and Water in Shale Inorganic Matrix. J Phys Chem C 2018;122(46):26671–9.
[30] Zhan SY, Su YL, Jin ZH, Wang WD, Li L. Effect of Water Film on Oil Flow in Quartz Nanopores from Molecular Perspectives. Fuel 2020;262:116560.
[31] Li P, Sun W, Wu B, Gao Y, Du K. Occurrence Characteristics and Influential Factors of Movable Fluids in Pores with Different Structures of Chang 6(3) Reservoir, Huaqing Oilfield, Ordos Basin, China. Marine Petrol Geol 2018;97:480–92.
[32] El Sharawy MS, Gaafar GR. Impacts of Petrophysical Properties of Sandstone Reservoirs on their Irreducible Water Saturation: Implication and Prediction. J Afr Earth Sc 2019;156:118–32.
[33] Qiao J, Zeng J, Jiang S, Zhang Y, Feng S, Feng X, et al. Insights into the Pore Structure and Implications for Fluid Flow Capacity of Tight Gas Sandstone: a Case Study in the Upper Paleozoic of the Ordos Basin. Mar Pet Geol 2020;118:104439.
[34] Meng Z, Sun W, Liu Y, Luo B, Zhao M. Effect of Pore Networks on the Properties of Movable Fluids in Tight Sandstones from the Perspective of Multi-Techniques. J Pet Sci Eng 2021;201:108449.
[35] Qu Y, Sun W, Wu H, Huang S, Li T, Ren D, et al. Impacts of Pore-Throat Spaces on Movable Fluid: Implications for Understanding the Tight Oil Exploitation Process. Mar Pet Geol 2022;137:105509.
[36] Li P, Jia CZ, Jin ZJ, Liu QY, Zheng M, Huang ZK. The Characteristics of Movable Fluid in the Triassic Lacustrine Tight Oil Reservoir: a Case Study of the Chang 7 Member of Xin'anbian Block, Ordos Basin. China Marine and Petroleum Geology 2019;102:126–37.
[37] Lai J, Wang G, Wang Z, Chen J, Pang X, Wang S, et al. A Review on Pore Structure Characterization in Tight Sandstones. Earth Sci Rev 2018;177:436–57.
[38] Guo X, Huang Z, Zhao L, Han W, Ding C, Sun X, et al. Pore Structure and Multi-Fractal Analysis of Tight Sandstone Using MIP, NMR and NMRC Methods: a Case Study from the Kuqa Depression, China. J Pet Sci Eng 2019;178:544–58.
[39] Lai J, Wang G, Cao J, Xiao C, Wang S, Pang X, et al. Investigation of Pore Structure and Petrophysical Property in Tight Sandstones. Mar Pet Geol 2018;91:179–89.
[40] Zeng LB, Liu GP, Zhu RK, Gao ZY, Gong L, Lv WY. A Quantitative Evaluation Method of Structural Diagenetic Strength of Deep Tight Sandstone Reservoirs in Kuqa Foreland Basin. Acta Pet Sin 2020;41(12):1601–9.
[41] Zhang S, Zhang B, Zhu G, Wang H, Li Z. Geochemical Evidence for Coal-Derived Hydrocarbons and their Charge History in the Dabei Gas Field, Kuqa Thrust Belt, Tarim Basin. NW China Mar Petrol Geol 2011;28(7):1364–75.
[42] Shen Y, Lü X, Guo S, Song X, Zhao J. Effective Evaluation of Gas Migration in Deep and Ultra-Deep Tight Sandstone Reservoirs of Keshen Structural Belt, Kuqa Depression. J Nat Gas Sci Eng 2017;46:119–31.

[43] Kenyon W. Nuclear Magnetic Resonance as a Petrophysical Measurement. Nucl Geophys 1992;6(2):153–71.
[44] Guo J-C, Zhou H-Y, Zeng J, Wang K-J, Lai J, Liu Y-X. Advances in Low-Field Nuclear Magnetic Resonance (NMR) Technologies Applied for Characterization of Pore Space inside Rocks: a Critical Review. Pet Sci 2020;17(5):1281–97.
[45] Li J, Li X, Wu K, Feng D, Zhang T, Zhang Y. Thickness and Stability of Water Film Confined inside Nanoslits and Nanocapillaries of Shale and Clay. Int J Coal Geol 2017;179:253–68.
[46] Nishiyama N, Yokoyama T. Estimation of Water Film Thickness in Geological Media Associated with the Occurrence of Gas Entrapment. Proceedings of the Fourteenth International Symposium on Water-Rock Interaction, WRI 14. 7. 2013, pp. 620-623.
[47] Intermolecular and Surface Forces. In: Israelachvili JN, editor Intermolecular and Surface Forces (Third Edition). Boston: Academic Press; 2011.
[48] Gregory J. Interaction of Unequal Double Layers at Constant Charge. J Colloid Interface Sci 1975;51(1):44–51.
[49] Lai J, Wang GW, Xin Y, Zhou L, Xiao CW, Han C, et al. Diagenetic Facies Analysis of Tight Sandstone Gas Reservoir of Bashijiqike Formation in Kuqa Depression. Nat Gas Geosci 2014;25(07):1019–32.
[50] Wang Z, Pan M, Shi Y, Liu L, Xiong F, Qin Z. Fractal Analysis of Donghetang Sandstones Using NMR Measurements. Energy Fuel 2018;32(3):2973–82.
[51] Tokunaga TK. DLVO-Based Estimates of Adsorbed Water Film Thicknesses in Geologic CO2 Reservoirs. Langmuir 2013;29(9):3152–62.
[52] Pan Y, Huang Z, Guo X, Liu B, Wang G, Xu X. Study on the Pore Structure, Fluid Mobility, and Oiliness of the Lacustrine Organic-Rich Shale Affected by Volcanic Ash from the Permian Lucaogou Formation in the Santanghu Basin, Northwest China. J Pet Sci Eng 2022;208:109351.
[53] Wu S, Wang X, Yu Y, Yu Y, Zhang L, Mao RLVJG. Nanoconfined Gas Flow Behavior in Organic Shale: Wettability Effect. Geofluids 2022;2022:1549003.
[54] Zhu H-L, Wang S-F, Yin G-J, Chen Q, Xu F-L, Peng W, et al. Study of the Numerical Simulation of Tight Sandstone Gas Molecular Diffusion Based on Digital Core Technology. Pet Sci 2018;15(1):68–76.
[55] Li J, Zhao JZ, Fan YF, Cao Q, Wang Q, Hu WQ. Gas Migration Mechanism of Quasi-Continuous Accumulation in the Upper Paleozoic of Ordos Basin. Oil&Gas Geology 2013;34(05):592–600.
[56] Zhao WZ, Bian CS, Xu ZH. Similarities and Differences Between Natural Gas Accumulations in Sulige Gas Field in Ordos Basinand Xujiahe Gas Field in Central Sichuan Basin. Pet Explor Dev 2013;40(04):400–8.
[57] Zhang Q, Wang W-D, Kade Y, Wang B-T, Xiong L. Analysis of Gas Transport Behavior in Organic and Inorganic Nanopores Based on a Unified Apparent Gas Permeability Model. Pet Sci 2020;17(1):168–81.
[58] Huang H, Li R, Chen W, Chen L, Jiang Z, Xiong F, et al. Revisiting Movable Fluid Space in Tight Fine-Grained Reservoirs: a Case Study from Shahejie Shale in the Bohai Bay Basin, NE China. J Pet Sci Eng 2021;207:109170.
[59] Bai ST, Cheng DX, Wan JB, Yang L, Peng HL, Guo XK, et al. Quantitative Characterization of Sandstone NMR T2 Spectrum. Acta Petrolei Sinica 2016;37 (03):382-91+414.
[60] He Y, Wang RF, Zhang ZY, Wang RY, Yin S, He WL, et al. Pore Structure and Movable Fluid Characteristics of Tight Sandstone Reservoirs in the Upper Shihezi Formation in Hangjinqi Area, Ordos Basin. Bulletin of Geological Science and Technology 2022. https://kns.cnki.net/kcms/detail/42.1904.p.20220527.1607.001.html.
[61] Qu HJ, Yang B, Tian XH, Liu XS, Yang H, Dong WW, et al. The Primary Controlling Parameters of Porosity, Permeability, and Seepage Capability of Tight Gas Reservoirs: a Case Study on Upper Paleozoic Formation in the Eastern Ordos Basin, Northern China. Petrol. Sci. 2019;16(6):1270–84.
[62] Zhu F, Hu W, Cao J, Sun F, Liu Y, Sun Z. Micro/Nanoscale Pore Structure and Fractal Characteristics of Tight Gas Sandstone: a Case Study from the Yuanba Area, Northeast Sichuan Basin, China. Marine Petrol Geol 2018;98:116–32.
[63] Zang Q, Liu C, Awan RS, Yang X, Li G, Wu Y, et al. Occurrence Characteristics of the Movable Fluid in Heterogeneous Sandstone Reservoir Based on Fractal Analysis of NMR Data: a Case Study of the Chang 7 Member of Ansai Block, Ordos Basin, China. J Pet Sci Eng 2022;214:110499.
[64] Jiang TW, Sun XW. Development of Keshen Ultra-Deep and Ultra-High Pressure Gas Reservoirs in the Kuqa Foreland Basin, Tarim Basin: Understanding Points and Technical Countermeasures. Nat Gas Ind 2018;38(06):1–9.
[65] Yin XD, Jiang S, Chen SJ, Wu P, Gao W, Gao JX, et al. Impact of Rock Type on the Pore Structures and Physical Properties within a Tight Sandstone Reservoir in the Ordos Basin. NW China Petroleum Science 2020;17(4):896–911.
[66] Ye YP, Tang SH, Xi ZD, Jiang DX, Duan Y. Quartz Types in the Wufeng-Longmaxi Formations in Southern China: Implications for Porosity Evolution and Shale Brittleness. Mar Pet Geol 2022;137:105479.
[67] Qiao J, Zeng J, Ma Y, Jiang S, Feng S, Hu H. Effects of Mineralogy on Pore Structure and Fluid Flow Capacity of Deeply Buried Sandstone Reservoirs with a Case Study in the Junggar Basin. J Pet Sci Eng 2020;189:106986.
[68] Ma Z, Tan J, Zheng L, Ni C, Hu R, Ma J. Simulation Experiment of Fluid-Feldspar Sandstone Interactions and Their Implications for Tight Oil and Gas Exploration of the Yanchang Formation, Ordos Basin, China. Mar. Petrol. Geol. 2022;142:105737.
[69] Wilson MJ, Wilson L, Patey I. The Influence of Individual Clay Minerals on Formation Damage of Reservoir Sandstones: a Critical Review with Some New Insights. Clay Miner 2014;49(2):147–64.
[70] Abitkazy T, Du S, Xu F, Shi Y. Pore Structure Characterization of Clay Minerals in the Lower Karamay Formation Conglomerate Reservoir in the Junggar Basin and its Impact on Hydrocarbon Storage and Seepage. Acta Geol. Sin. - English Edition 2021;95(2):558–69.